LAWRENCE
LIVERMORE
NATIONAL
LABORATORY

LLNL-JRNL-663401

Direct simulation of a high convergence cryogenic implosion experiment on the National Ignition Facility

D. S. Clark

October 28, 2014

Physics of Plasmas

Disclaimer

This document was prepared as an account of work sponsored by an agency of the United States government. Neither the United States government nor Lawrence Livermore National Security, LLC, nor any of their employees makes any warranty, expressed or implied, or assumes any legal liability or responsibility for the accuracy, completeness, or usefulness of any information, apparatus, product, or process disclosed, or represents that its use would not infringe privately owned rights. Reference herein to any specific commercial product, process, or service by trade name, trademark, manufacturer, or otherwise does not necessarily constitute or imply its endorsement, recommendation, or favoring by the United States government or Lawrence Livermore National Security, LLC. The views and opinions of authors expressed herein do not necessarily state or reflect those of the United States government or Lawrence Livermore National Security, LLC, and shall not be used for advertising or product endorsement purposes.

Direct simulation of a high convergence cryogenic implosion experiment on the National Ignition Facility

D. S. Clark, M. M. Marinak, C. R. Weber, D. C. Eder, S. W. Haan, B. A. Hammel, D. E. Hinkel, O. S. Jones, J. L. Milovich, P. K. Patel, H. F. Robey, J. D. Salmonson, S. M. Sepke, and C. A. Thomas

Lawrence Livermore National Laboratory, Livermore, CA 94551

Abstract

The recently completed National Ignition Campaign (NIC) on the National Ignition Facility (NIF) showed significant discrepancies between post-shot simulations of implosion performance and experimentally measured performance, particularly in thermonuclear yield. This discrepancy between simulation and observation persisted despite concerted efforts to include all of the known sources of performance degradation within a reasonable 2-D, and even 3-D, simulation model, *e.g.*, using measured surface imperfections and radiation drives adjusted to reproduce observed implosion trajectories [D. S. Clark *et al.*, Phys. Plasmas **20**, 056318 (2013)]. Since the completion of the NIC several effects have been identified that could explain these discrepancies and that were omitted in previous simulations. In particular, there is now clear evidence for larger than anticipated long-wavelength radiation drive asymmetries and a larger than expected perturbation seeded by the capsule support tent. This paper describes an updated suite of 1-D, 2-D, and 3-D simulations that include the current best understanding of these effects identified since the NIC, as applied to a specific NIC shot. The relative importance of each effect on the experimental observables is compared. While the agreement with the experimental data is not perfect, the comparison to the data is significantly improved, suggesting that the leading effects responsible for the yield degradation have been captured.

I. INTRODUCTION

The National Ignition Campaign (NIC) [1] on the National Ignition Facility (NIF) [2] was completed in September 2012. While substantial progress was made in experiments on NIF, the NIC ultimately fell short of its goal of demonstrating ignition by indirect drive inertial confinement fusion [3, 4]. Implosions driven by record-breaking laser powers and energies on NIF and tuned with unprecedented precision and control achieved implosion velocities of 350 km/s, deuterium-tritium (DT) fuel densities of greater than 800 g/cm^3, and fuel areal densities greater than 1.3 g/cm^2. Nevertheless, DT fusion yields did not exceed ~ 9×10^{14} neutrons, well below the ~ 5×10^{16} threshold of unambiguous fusion ignition. This leaves the obvious question: why did NIC implosions perform so much lower than expectations?

In parallel to the experimental campaign conducted during NIC, a concerted effort was also undertaken to model NIC experiments in as much detail as possible [5, 6] using the HYDRA radiation hydrodynamics code [7]. These simulations were run in a manner similar to the simulations used in designing the original ignition point design but included as much as possible any variations in the target geometry or laser drive particular to a given experiment. Across the full range of pulse shapes and target geometries explored during NIC, these detailed post-shot simulations consistently over-predicted implosion yields by factors from 3 – 10. Given residual uncertainties in the experimental conditions, the simulations could be adjusted within those uncertainties to match approximately the measured areal densities, ion temperatures, and x-ray images sizes, among other properties, but the discrepancy in yield was consistent and applied even in the case of state-of-the-art, high-resolution, three-dimensional (3-D) simulations. Interestingly, similar discrepancies between simulation and experiment have been reported in modeling cryogenic direct-drive implosions [8] on the Omega laser system [9].

Since these simulation studies were completed, experiments have continued on NIF and have identified several important effects—absent in the previous simulations—that have the potential to resolve at least some of the large discrepancies between simulated and experimental yields. Briefly, these effects include larger than anticipated low-mode distortions of the imploded core—due primarily to asymmetries in the x-ray flux incident on the capsule—, a larger than anticipated perturbation to the implosion caused by the thin plastic membrane or "tent" used to support the capsule in the hohlraum prior to the shot, and the presence, in some cases, of larger than expected amounts of ablator material mixed into the hot spot. The purpose of this paper is to describe updated simulation results accounting for these effects identified since the NIC. The goal of this study is to determine whether the standard simulation paradigm, the same paradigm and methods used in designing the initial ignition targets for NIF and still used in modeling current and future NIF experiments, is adequate to explain implosion performance once all of the important effects have been included. Only by a serious accounting for all of the effects definitely known to have been present in NIC implosion experiments can the standard simulation methodology be judged against its ability to model the experimental data. If large discrepancies remain between simulations and experimental results, even after all of the currently known effects have been included, then clearly the search must continue for additional degradation sources that must be influencing implosion performance. On the other hand, if substantial agreement is found with the data, then in some limited sense the standard methodology can be judged adequate. While the agreement with the data is imperfect, the conclusion to be drawn from the simulations presented below is closer to the latter case. That is, once these large effects that were overlooked in previous simulations are properly accounted for, the discrepancies found with previous simulations are largely resolved.

The progress of the NIC is globally summarized in Fig. 1, where implosion performance is plotted in the plane of neutron yield versus fuel areal density. Here the blue symbols represent the "low foot" shots fired during the NIC [1], and the green symbols present "high foot" shots fired since the NIC [10]. The dashed lines are contours of yield amplification due to α-particle self-heating as predicted from simulations, and the blue and green arrows, respectively, indicated the progress of the campaigns over time. The first cryogenic implosion experiment was carried out on NIF on Sept. 29, 2010 [11]. Following the NIF shot nomenclature of NYYMMDD, this shot is designated N100929. This shot was conducted prior to any of the implosion tuning experiments planned to adjust the implosion shock timing and low-mode implosion symmetry empirically [12]. Given that the implosion design codes were not expected to be accurate enough to predict these tuning adjustments *a priori* and experimental campaigns were planned to conduct this tuning empirically, it was not surprising that the performance of this first implosion was relatively poor. Over the following eighteen months, the planned implosion tuning campaign was carried out as part of the NIC resulting in significant improvements in both implosion yield and confinement. This phase of the NIC culminated in shot N120321 that reached a record fuel areal density of 1.3 g/cm^2 and a yield of 4.1×10^{14} [13]. This shot used a 1.5 MJ/320 TW laser pulse in a 5.75 mm diameter uranium hohlraum with a 4.0 at. % Si-doped plastic capsule. While this shot achieved an areal density close to the ignition goal of 1.4 g/cm^2, the neutron yield was nonetheless significantly lower than expectations. Subsequent attempts to further improve implosion performance from N120321 unfortunately were not successful and resulted in degradations in yield, degradations in confinement, or both. In this sense, N120321 represented the "high water mark" of NIC.

Following the conclusion of the NIC, the "high foot" campaign began on the NIF [10]. These

implosions use a higher radiation temperature during the first stage of the x-ray pulse shape ("the foot") and otherwise implode a similar fusion capsule with a similar peak x-ray drive as those fired during the NIC. Motivated by design studies undertaken during the NIC [14] that showed the potential for significantly reduced Rayleigh-Taylor [15, 16] and Richtmyer-Meshkov [17, 18] instability growth in high foot-type implosions, this approach was not pursued during the NIC due to the accompanying loss in compression in this type of implosion. The reduced compression achieved in high foot implosions as compared to the NIC low foot implosions is evident from the green symbols in Fig. 1, where areal densities are much as 50% lower than those with the low foot. Nevertheless, likely due to their improved hydrodynamic stability, these implosions have achieved an order of magnitude improvement in neutron yield compared to the low foot implosions. When fired at the highest allowable laser powers, the high foot approach has finally crossed into the α-particle self-heating regime [19] as indicated by crossing the "α-dominated" contour in the figure. Achieving ignition at the NIF energy scale, however, will likely require a combination of the best features of both of these implosion approaches, achieving hot spot self-heating by α-particle deposition and an areal density approaching 1.4 g/cm^2. While progress along the trajectory of the high foot campaign is valuable and encouraging, understanding the performance and, in particular, failure modes of the higher compression low foot shots is therefore also crucial. Only by understanding the behavior of the high convergence, high compression implosions fired during the NIC is there a prospect of successfully combining the high compressions reached in these shots with the higher yield shots of the high foot campaign. As the highest compression shot yet fired on NIF, much effort has then focused on gaining a detailed understanding of shot N120321, and modeling this shot is the exclusive focus of this paper.

This paper is organized as follows. Section II reviews in more detail the degradation mechanisms identified since the conclusion of the NIC and absent in previous simulations of N120321. Section III then describes a hierarchy of one-dimensional (1-D) and two-dimensional (2-D) simulations in which these effects are added incrementally to illustrate the relative importance of each effect in determining the aggregate implosion performance. Section IV then describes the state of three-dimensional (3-D) simulations of N120321 analogous to the 2-D simulations of Sec. III. The important role of viscosity in the flow dynamics of the hot spot, as recently identified elsewhere [20], is also discussed. Section V concludes.

II. DEGRADATION SOURCES IDENTIFIED SINCE THE NIC

As already mentioned in Sec. I, three leading perturbation sources, omitted in previous simulations of NIC implosions, have been identified by NIF experiments subsequent to the NIC. Each of these is discussed in more detail here. Since this study was undertaken, some evidence has also arisen suggesting an additional perturbation source other than the three specifically considered here. That is, larger than anticipated fuel pre-heat due to energetic electrons produced from laser-plasma interactions in the hohlraum [21]. While this is an important effect to consider in any detailed post-shot model, the magnitude of this effect remains a subject of debate and the possible role of hot electrons will not be considered further here. Once consensus is reached on the magnitude of this effect, based on future NIF experiments, then it can be included in future simulations.

A. Low-mode shape distortions

The first large degradation source identified since the NIC was large low-mode distortions of the implosion shape. That is, deviations of the implosion shape in-flight or at stagnation from

the symmetric, round ideal and typically characterized as large amplitudes in the first two even Legendre modes, P_2 and P_4. The first clear indication of larger than expected low-mode distortions in the imploded fuel configuration derived from nuclear activation measurements using zirconium threshold detectors [22]. These measurements used seventeen zirconium "pucks" placed around the target chamber to record the neutron fluence in each of these seventeen directions. Where the activation recorded by a puck is high, the scattering of the neutrons emitted by an assumed central source must be low and the corresponding fuel areal density must be low. Conversely, where the activation is low, the scattering must be large and the areal density high. Although the coverage of the 4π steradians of the target chamber is sparse with only seventeen sampling points, it is possible to fit the activation data to a second order Legendre decomposition and from this infer the low-mode fuel asymmetry averaged over the burn duration. Such fits are consistent with areal density fluctuations of up to 50% about the mean for some shots. Clearly, this represents a large, and unacceptable, asymmetry in the imploded fuel.

Motivated by these inferred fuel asymmetries, a dedicated experimental campaign was undertaken after the conclusion of the NIC to measure the in-flight shell asymmetries in NIC-type implosions [23]. In these experiments, 10 keV x-rays from a germanium backlighter were used to image a surrogate capsule implosion in both the equatorially and polar directions. From the resulting radiographs, fits can be made to the imaged minimum transmission contour and imaged limb minimum. Legendre decomposing these fits and comparing to simulations indicated a larger than expected P_4 or diamond-shaped asymmetry in NIC-type implosions at a radius of ~ 200 μm [24]. According to simulations, perturbations of this magnitude can be expected to degrade implosion yield by a factor of two [25]. While the precise origin of the

responsible asymmetries in the hohlraum radiation flux has yet to be fully identified and a strategy for controlling it found, these radiography data are nonetheless sufficient to enable "tuning" the radiation drive used in the simulations to match the observed asymmetry data. The impact of this tuning on the simulated results is described in more detail below.

B. The capsule support tent

An important and fortuitous discovery also made from the backlit implosion experiments used to diagnose implosion shape was the unexpectedly large perturbation seeded by the capsule support tent [26]. Prior to the shot, the capsule is supported in the center of the hohlraum by a pair of thin plastic membranes with a thickness of 110 nm in the case of N120321. These "tents" envelop either pole of the capsule and peal away from the surface of the capsule at a polar angle of roughly 45°. In in-flight radiographs taken as part of the low-mode shape measurements, this 45° separation point is remarkably coincident with a clear "scar" across the face of the corresponding in-flight radiograph. To confirm that in fact the tent is responsible for this visibly large perturbation, a shot was fired with the capsule supported by a 30 μm thick stalk as opposed to the conventional tent. While this would seed too large a perturbation to be viable for an ignition capsule at full convergence, the absence of the "tent scar" from this surrogate implosion clearly confirmed that the tent is the source of this perturbation. By contrast, according to previous simulation-based estimates, the tent should have produced an essentially invisible perturbation in such radiographs. Furthermore, simulations deliberately perturbed so as to reproduce the radiographic signatures attributed to the tent showed a yield degradation of roughly a factor of two from this effect alone. Again, while the exact hydrodynamics of how such a fine-scale feature as the support tent seeds the large perturbations seen in radiographs remains an area of active research, surrogate perturbations can nevertheless

be tuned into simulations to capture the gross effect of the tent on performance. This surrogate perturbation will be described in more detail below.

C. Mix of ablator material into the hot spot

An additional effect omitted in previous systematic simulations of NIF implosion performance is the presence of deeply penetrating mix contaminating the DT hot spot with higher *Z* ablator material. While the effects of this "deep mix" have long been appreciated based on simulations [27, 28] and significant efforts have been made to measure it using tracer spectroscopy [29], sufficiently detailed shot-by-shot data on deep mix was only just becoming available at the time previous simulation studies were being run. Some scoping studies [6] and attempts to connect the inferred mix from NIF experiments to target quality were made [30], but only relatively recently has a systematic analysis based on Ross pair x-ray images of NIF implosions produced a fairly comprehensive database on deep mix in NIC implosions [31].

These inferred mix masses are derived from combined measurements of neutron and x-ray yield [31]. In outline, the hot spot x-ray yield is a function of the hot spot density, hot spot temperature, hot spot <*Z*> or contamination fraction, hot spot size, and optical depth of the surrounding ablator. Likewise, the neutron yield of the hot spot is a function again of the hot spot density, hot spot temperature, and hot spot size. Neglecting gradients or other shape details, the ratio of x-ray to neutron yield is then only a function of the hot spot temperature, the optical depth of the surrounding material, and the amount of higher *Z* contamination in the hot spot. Assuming that the hot spot temperature is adequately characterized by the ion temperature inferred from the Doppler width of the emitted neutron spectrum and estimating the ablator optical depth from energy-resolved x-ray emission measurements, the hot spot contamination

can then be inferred. These mix estimates still have considerable uncertainty and the origins of the large amounts of mix inferred on many NIF shots remains unexplained, but the presence of this mix is a clearly a non-negligible effect in many NIF implosions and must be included in any plausible simulation model.

III. 2-D SIMULATIONS AND HIERARCHY OF DEGRADATION SOURCES

Bearing in mind the degradation sources discussed above, this section describes a sequence of simulations in which each of these effects is added in turn to assess their relative importance in determining the final simulated implosion performance. The simulations discussed in this section are 1-D (symmetric) or 2-D, as asymmetric effects are included. The following section describes similar simulations but extended to 3-D.

The 2-D simulations of N120321 comprising this study follow essentially the same methodology as described in Ref. [6]. These capsule-only simulations are run with the radiation hydrodynamics code HYDRA [7] and use roughly 450 radial by 1000 angular zones across the complete 180° extent of the capsule in polar angle. This resolution is sufficient to capture perturbation growth at wavelengths as small as those characterized by Legendre mode numbers $\ell = 100$ and has been found adequate to capture the effects of broad spectrum roughness. As-measured outer ablator surface and inner DT ice roughnesses are used as perturbation seeds in the $\ell = 1 - 100$ range, and nominal roughness specifications are used to initialize all of the internal, unmeasured interfaces [28]. Multi-group diffusive radiation transport is included with sixty radiation groups, single-group electron and ion conduction is included, and tabular equations of state, opacities, and thermal conductivities are used. Particle Monte Carlo (PMC) transport is used for fusion burn products with typically 150,000 particles tracked, and α-

particle momentum and energy deposition are included in all of the simulations described here. Also like the simulations described in Ref. [6], the simulations of N120321 described here used x-ray sources to drive the capsule implosion that have been tuned to match several measured 1-D characteristics of the implosion: the x-ray source is adjusted to match very accurate shock timing measurements taken by VISAR [32], measurements of the capsule implosion velocity from convergent ablator measurements [33], and finally the time of peak neutron production ("bang time") from the DT shot itself. Unlike the x-ray sources discussed in Ref. [6], note that the x-ray source used in the simulations discussed here was not adjusted to match the measured neutron down scattered ratio (DSR), a measure of the burn-averaged compression achieved in the implosion [34]. In Ref. [6], the end of the x-ray source was truncated to reduce the simulated DSR to match the measured value for each shot. The x-ray source used in the simulations here is not truncated and so overshoots the measured DSR in 1-D. Given the enhanced perturbations now included in the 2-D simulations in this study, it is found that the DSR is sufficiently degraded in 2-D that the simulations approximately match the measured value without the 1-D degradation used previously. Also different from the x-ray sources used in Ref. [6], the hard x-ray fraction in the source (the fraction of the incident x-ray energy with $h\nu > 1.8$ keV, also referred to as the M-band fraction) was adjusted to agree with recent measurements of the M-band fraction using the NIF View Factor platform [35]. This results in an M-band fraction of approximately 18.5% at a radiation brightness temperature of 300 eV. This adjustment of the M-band fraction was found necessary for simulations to match observed ablation front Rayleigh-Taylor growth rates measured in Hydrodynamic Growth Radiography (HGR) experiments also recently completed on NIF [36, 37, 38]. In this sense, the simulations described here have been shown to be largely consistent with measured ablation front instability

growth rates from dedicated NIF measurements.

To account for the degradation sources discussed in Sec. II, the following additions were made to the simulations. First, radiation flux asymmetries for modes P_2 and P_4 were included that were deliberately tuned to match companion in-flight shape measurements. Similar low-mode asymmetries were included in the simulations in Ref. [6], but these were based on hohlraum simulations that have since been found to underestimate the magnitude of the flux asymmetries in these modes.

Second, a surrogate perturbation was added to the ablator surface to reproduce the radiographic signature seen in backlit imaging and attributed to the support tent. Such a fine-scale feature as the support tent (~ 100 nm thick) cannot be resolved in the standard resolution simulations described here and can only be fully captured in specialized, very high resolution simulations dedicated to resolving this effect [39]. Since these fully resolved simulations are too computationally expensive to run in but a few specialized cases, the surrogate perturbation must be used. By comparing simulated radiographs to the defects captured in in-flight radiographs, a cosine shaped groove 350 μm in width at its base and 200 nm deep was found to mimic best the in-flight perturbation attributed to the tent [40]. As described below, this perturbation alone amounts to a yield reduction of more than a factor of two in simulations.

Third, 200 ng of doped ablator material was "pre-mixed" into the DT gas in the center of the capsule at the start of the simulation to mimic the effect of deep mix into the hot spot at late times. In the actual implosion experiment, it is expected that this ablator material is injected into the hot spot in the highly nonlinear, high aspect ratio jets that can arise from localized defects (bumps, divots, or dust particles) present on the ablator surface as seen in simulations

[27]. Such simulations are again too computationally expensive to run except in specialized cases and currently impossible to run in 3-D, as would be appropriate to capture the true random distribution of defects around the capsule surface. In 2-D simulations, these localized defects can also only be properly treated as located at the poles, which artificially confines this source of mix to two locations in the simulation. On account of these limitations, the expediency of pre-mixing the ablator material into the central gas has been adopted. This incurs the inevitable shortcoming that the mixed ablator material is present in the hot spot throughout the simulation and does not "arrive" in the hot spot at the physically appropriate time late in the implosion. Furthermore, if the mix mass is initialized only in the central gas, it can be artificially compressed into a very small, albeit highly distorted, region in the very center of the hot spot and not more plausibly mixed throughout the hot spot formed by both the initial DT gas and DT ice that is ablated from the inner edge of the ice layer. For mix masses greater than ~ 100 ng, this can result in an unphysical densification, due to radiative collapse, in the very center of the hot spot. For this reason, the simulations described here divide the mix mass between the initial DT gas and the inner 3.5 μm of DT ice that ultimately forms the remainder of the hot spot. This initialization much more evenly spreads the mixed material through the eventual hot spot and gives a more physically plausible simulation of the mix hot spot conditions.

Particular to N120321, depending on what assumptions are made, estimates of the hot spot mix mass based on the x-ray measurements have ranged from ~ 400 ng to less than the detection threshold of ~ 100 ng. The simulations described here all assume 200 ng of ablator material was mixed into the hot spot. Unfortunately, there remains uncertainty in the precise amount of ablator material that entered the hot spot on any given shot, and, given the high sensitivity of simulated yields to the amount of hot spot contamination, there therefore remains uncertainty in

the simulated results. The results shown below nonetheless show a plausible consistency with the measured implosion characteristics assuming the 200 ng used here. Note that current simulations can account for only 50 – 100 ng of ablator mix into the hot spot under worst-case assumptions; however, recent very high resolution simulations aimed at resolving the effect of the capsule support tent show > 400 ng of ablator material reaching the hot spot for a higher power companion shot to N120321 [39]. It is not unlikely then that 100 – 200 ng of ablator material mixed into the hot spot on shot N120321.

Finally, although known as a degradation source since before the start of the NIC but not included systematically in previous simulations, a surrogate perturbation for the capsule fill tube has been included in the simulations in this study. Like the support tent or localized surface defects, the fill tube is too small of a feature to resolve in standard simulations and can only be captured in simulations currently too costly to run but in specialized cases. A surrogate perturbation consisting of a 300 nm deep by 15 μm wide Gaussian divot is then initialized at the pole to model the fill tube effect. In isolated simulations, this produces a similar perturbation to fully resolved simulations and injects ~ 25 ng of ablator material into the hot spot similar to the results of the fully resolved simulations. As shown in Fig. 2 below, the presence of this type of fill tube perturbation significantly changes the hot spot morphology and therefore should not be neglected in any plausible simulation of this type of implosion.

To assess first the individual impact of each of the degradation sources discussed above, Fig. 2 shows the results of 2-D simulations including each of the above effects individually. In each of the six panels, the upper half shows the material density at bang time, while the lower half shows the material regions, with dark and light blue denoting the DT gas and DT ice, respectively, and the other colors the various doped ablator layers. The hohlraum symmetry

axis is horizontal in this and the following figure. All of the panels use the same density color scale given on the right, and the red contour drawn over each panel traces the hot spot boundary following a standard definition [41]. The inset in each panel also lists the simulated values for four of the principle experimental observables: the x-ray image size or P_0 as determined from the 17% image intensity contour in the equatorial direction, the down scattered ratio of neutrons in the 10 – 12 MeV energy band to the primary 13 – 15 MeV band, the ion temperature as extracted from the width of the primary neutron energy spectrum, and finally the primary neutron yield in the 13 – 15 MeV band. The upper left panel shows the result of the unperturbed (1-D) clean simulation, while the upper center panel shows the result of adding 200 ng of ablator mix into the hot spot. Note that this simulation includes an added material region compared to the other panels to account for the region on the inner edge of the DT ice that includes half of the ablator mix mass. The upper right panel shows the result of including the P_2 and P_4 flux asymmetries alone, while the lower left and lower center panels show the individual impacts of the surrogate fill tube perturbation alone and the surrogate tent perturbation alone. Finally, the lower right panel shows the effect of the surface roughness (ablator, DT ice, and all internal interfaces) alone. Focusing only on the primary yield values, the presence of the mix mass in the hot spot center can be seen to account for the largest yield degradation relative to the unperturbed, clean simulation. Following the mix mass, the low-mode flux asymmetries and surrogate fill tube perturbation are seen to have very similar impacts on the yield and slightly less than the impact of the mix mass. The surrogate tent perturbation is a somewhat weaker source of yield degradation yet, while the surface roughness is the weakest source of yield degradation of all.

The implosion experiment, of course, includes all of these effects simultaneously. A sense of

the cumulative effect of all of these degradation sources is given in Fig. 3 in which each of the effects is added incrementally to the others going from left to right and top to bottom. The upper left and center left panels simply repeat from Fig. 2 showing the unperturbed, clean simulation results and the result of adding the ablator mix mass to the hot spot. The upper right panel then adds the low-mode flux asymmetries in addition to the mix mass, while the lower row successively adds the effects of the fill tube, the support tent, and finally the surface roughness. Again focusing only on the yield, what is evident is the apparent saturation of the impact on the yield once more than three effects are included together. That is, once the mix mass and shape distortions are accounted for, including one more degradation mechanism effectively saturates the simulated yield. What is also apparent from the lower center panel is the effectively nonlinear combination of the effect of the tent perturbation with the low mode shape. The thinning of the shell due to the low-mode flux asymmetries damagingly coincides with the location of the tent perturbation in such a way that the hot spot distortion due to the tent is strongly magnified when compared to the tent alone simulation in Fig. 2.

A summary of these individual and cumulative impacts as compared to the data is given in Fig. 4. In each of the panels, the simulated value of one of the principle observables (Y_n, T_{ion}, DSR, and x-ray P_0) is plotted as a function of degradation source. The blue bars give the simulation results for each effect individually, while the red bars show the cumulative impact of adding each effect from left to right. The experimental value for each of the observables with its associated error bar is given by the pink band. From the blue bars, it is again apparent that the ablator mix mass in the hot spot has the strongest impact on all of the observables with the possible exception of the x-ray image size. After this, the low-mode flux asymmetries and fill tube perturbation have the largest impact on all observables except for the DSR. From the red

bars, it is interesting that the cumulative simulations including all effects match all of the observables within the error bars except for the neutron yield, which is high by a factor of three. It is also interesting that this level of agreement nearly applies to all of the cumulative simulations that include at least the mix mass, shape, and the fill tube. This again emphasizes the saturating effect of having several degradation sources adding on top of one another.

IV. 3-D SIMULATIONS

Despite 2-D simulations matching the measured ion temperature, down scattered ratio, and x-ray image size, as shown in Fig. 4, a factor of three discrepancy remains in the simulated yield. This section describes 3-D simulations analogous to the 2-D simulations of Sec. III aimed at resolving this remaining yield discrepancy and also providing insight into the genuinely 3-D character of high convergence NIF implosions. Clearly, fully 3-D simulations enable a more faithful representation of the 3-D initial conditions present in the experiment. That is, the 3-D perturbations that are inevitably present on the capsule surfaces (bumps, divots, and scratches on the ablator surface and grooves in the DT ice layer), as well as in the x-ray flux on the capsule, can be represented as such without any of the approximations necessary to mimic these effects in 2-D. Even more importantly, 3-D simulations covering the entire sphere remove the artificial symmetry present in 2-D simulations that tends to exaggerate the stagnation effect in a converging flow, such as an ICF implosion. 2-D symmetry also suppresses the more chaotic, turbulent-like structures that naturally arise in 3-D.

The first 3-D simulations of indirect drive implosions using HYDRA were reported in Refs. [42, 43, 44, 45, 7, 46, 47]. These all focused on 3-D subsectors of the capsule and did not cover the complete sphere. The first full sphere capsule simulations using HYDRA were reported in

Ref. [48]. These simulations used a sliding Eulerian mesh and zonal mass perturbations as initial conditions. The first 3-D arbitrary Lagrangian-Eulerian (ALE) simulations run with HYDRA covering the full spherical extent of the capsule were described in Ref. [6]. 3-D full sphere simulations have also been run using the RAGE code [49] but so far for lower convergence implosions than those modeled here [50]. The 3-D full sphere simulations described here and in Ref. [6] use the same perturbation seeding scheme and similar ALE mesh handling as the 2-D simulations in Sec. III but extended to 3-D. In this sense, these simulations represent the best practices for resolving the hydrodynamics of instability growth in these high convergence, Rayleigh-Taylor unstable implosions.

Similar to the 3-D simulations of Ref. [6], the 3-D N120321 simulations described here used as much of the pre-shot capsule metrology data as are available as initial conditions. These data include ablator outer surface maps taken from Atomic Force Microscopy (AFM) traces for low modes ($\ell < 20$) [51] and Phase-Shifting Diffraction Interferometer (PSDI) maps for higher modes ($\ell > 20$) [52]. X-ray imaging of the DT ice layer prior to the shot provides DT ice roughness spectrum data, low-mode 3-D shape data ($\ell, m < 8$), and also the 3-D distribution of more localized ice grooves [53] that were all incorporated into the simulations. In addition to the 2-D x-ray flux asymmetries used in the simulations in Sec. III, the 3-D simulations also incorporate 3-D flux asymmetries extracted from a companion 3-D hohlraum simulation to account for the 3-D effects of as-shot beam imbalance, mis-pointing, etc. Note that, while these initial conditions represent the most detailed representation of the perturbation seeds present in any implosion simulation to-date, the relative orientations of these perturbations are unfortunately not absolutely known. That is, while there is detailed knowledge of the structure of the surface perturbations, between the time that the PSDI and AFM measurements are

recorded and the time the capsule is assembled, an essentially arbitrary rotation is introduced between the mapped surface features and the known locations of the fill tube, tent, flux asymmetries, etc. In this sense, the initial conditions for the simulation represent the best that can be achieved with the surface characterizations that are available, but uncertainties inevitably remain.

Compared to Ref. [6], what is different in the simulation setup here is that the added degradation sources described in Sec. II have now also been included. That is, 3-D analogs of the surrogate tent and fill tube perturbations have been added, and the same 200 ng of ablator mass has been pre-mixed into the central DT gas. Note that in these 3-D simulations, the ablator mix mass has been initialized only in the DT gas and not in both the DT gas and inner ice, and the added mixing anticipated in 3-D is relied on to distribute the mix mass thoroughly through the hot spot volume. Also advantageous in the 3-D simulations, the fill tube perturbation is correctly located at the waist of the capsule and not at the pole as required in 2-D. This sets the proper orientation of this perturbation with respect to the tent perturbation and x-ray flux asymmetries, as well as with respect to the simulated diagnostic lines of sight discussed below. Finally, as an additional improvement over the 3-D simulation in Ref. [6], the resolution has been increased from the previous $\ell = 50$ resolution to the same $\ell = 100$ resolution as used in the 2-D simulations of Sec. III. This increased resolution inevitably comes at the price of increased computational cost, and the simulations described here require ~ 400 million computational zones (400 radial by 1000 angular zones in each direction) and ~ 4.5 million CPU-hours or ~ 1 month on 6,000 CPUs to complete.

The aggregate of the initial conditions used for the N120321 3-D simulation is illustrated in Fig. 5. Fig 5(a) shows the DT ice-gas interface as initialized in the simulation with the color

scale showing the height deviation around the surface relative to the average. The combined effect of low-mode distortions of the interface, higher-mode roughness, and the localized groove-type defects is apparent. Fig. 5(b) is an analogous plot for the initial outer ablator surface and shows the combined perturbations due to the low-mode AFM roughness, higher-mode PSDI roughness (that includes the more localized surface defects) and the large surrogate tent perturbation.

Fig. 6 shows a sequence of renderings from the 3-D simulation during the later phase of the implosion. In each of the snapshots, the outer green surface is the interface between the inner DT fuel and the outer plastic ablator. This surface has been cut away with the color scale of the left cutaway showing the fluid flow speed and the color scale of the right cutaway showing the material density. The hohlraum axis is vertical in this and the following figure. The first snapshot (t = 22.53 ns) shows the state of the simulation shortly after peak implosion velocity when the main stagnation shock that decelerates the dense shell is just becoming evident. Several other features are also apparent: On the outer fuel-ablator interface, the surrogate tent perturbation can be seen to have cut large grooves around each pole, while the other ablator surface defects have grown and fed through as spike-like defects on the fuel-ablator interface. Likewise, the surrogate fill tube perturbation has caused a jet of ablator material to begin to fall into the hot spot at the waist of the implosion. What is most striking in this rendering, however, is the highly structured and very high velocity flows that have arisen in the low density hot spot region at this time. As shown by the color scale on the left, these flows have reached localized velocities exceeding 500 km/s, significantly greater than the overall fuel implosion velocity of ~ 330 km/s, and have produced very fine-scale, turbulent-like structures in the low-density, nascent hot spot. Following this simulation more closely in time shows that these fine-scale hot

spot flows grow rapidly during the multiple reverberations of the main implosion shock as it rebounds from the center of the implosion. The small distortions in the shock front due to the initial ablator surface roughness and other irregularities are rapidly amplified with each of the roughly half dozen reflections of this shock between the dense shell and the implosion center leads to the very structured hot spot flow seen in the figure.

In the next snapshot (t = 22.65 ns), the shell deceleration and stagnation are well underway and the shell density has increased to ~ 120 g/cm^3. The tent perturbation can be seen to have seeded deceleration phase Rayleigh-Taylor growth at the boundary of the forming hot spot with weakly nonlinear spikes of dense DT falling into the hot spot while a thinning of the shell and rising bubble of low-density hot spot forms in between. The fill tube perturbation has now effectively jetted ablator material to the very center of the hot spot, while the turbulent-like flows continue in the low density hot spot region as they are compressed by the surrounding dense shell. Note that the density color scale and length scale have changed in this rendering, but the speed color scale is the same.

The third snapshot (t = 22.83 ns) shows the state of the simulation at bang time. At this time, the small-scale hot spot flows appear to have collimated into a larger-scale and more coherent jet-like flow directed along the z-axis of the implosion and somewhat toward the upper left corner in the figure, through the gap in the dense shell seeded by the tent defect. The effect of the low-mode flux asymmetries can also be seen to have turned an initially spherical implosion into a highly prolate one by this time. Finally, the last snapshot (t = 22.96 ns) shows the state of the implosion at the end of the simulation when the fusion reaction rate has dropped to less than one tenth of one percent of its peak. The high velocity jet appears to have "vented" the hot spot through the breach caused by the support tent but over a relatively narrow range in azimuth,

while the low-mode flux asymmetries have left two dense polar caps in the imploded fuel configuration. Note that the venting of the hot spot through a relatively narrow region in azimuthal represents a uniquely 3-D failure mechanism that cannot occur in a 2-D, axisymmetric configuration. In this case, the hot spot disassembly appears to result from a coincidence of the tent defect with a localized 3-D defect on the ablator surface, or possibly a 3-D x-ray drive asymmetry, again a uniquely 3-D effect. While it is impossible to be certain that such a collusion of effects actually happened on N120321 (especially given the lack of data on the absolute orientation of the ablator surface defects relative to the tent defect), the fact that such a failure is possible, and possible only in 3-D, is important to recognize for understanding the behavior of real 3-D implosion experiments.

The simulation shown in Fig. 6 was run without including physical viscosity, as is typical for ICF simulations run in HYDRA or other codes. Recently, however, it was shown [20] that physical viscosity plays a very strong role in damping precisely the small scale, high velocity flows that are so evident in the earlier time snapshots of Fig. 6. To assess the role of physical viscosity in these simulations of N120321, the simulation from Fig. 6 was restarted shortly before the time of shock convergence at the implosion center (t = 21.4 ns) with physical viscosity included. In this case, the physical viscosity model was that described by Ref. [54], essentially a Braginskii viscosity with modifications for degenerate plasmas. Fig. 7 compares the results of the previous inviscid simulation shown in Fig. 6 against the results with physical viscosity at the representative times of t = 22.53 ns (peak implosion velocity) and 22.83 ns (bang time). Comparing the inviscid simulation in the left column to the viscous simulation in the right column shows the dramatic smoothing of the small-scale flow structures that occurs early in time when viscous dissipation is included. The bulk structure of the flow, including the

inward penetration of the fill tube jet into the low density hot spot appears not to be significantly modified; however, the finer-scale, high speed features in the center of the inviscid simulation have been completely wiped away. At bang time, interestingly, the differences between the inviscid and viscous simulations have become somewhat more muted. As described above, in the inviscid simulation, the small-scale flow features appear to have collimated into a more coherent jet-like structure by bang time, and this jet structure appears to be largely reproduced in the viscous simulation. Some of the finer-scale secondary flows around the jet have been dissipated by viscosity, but the differences are much less stark than in the earlier time comparison.

A clearer picture of the differences between viscous and inviscid simulations, and also between the 2-D simulations of Sec. III and the 3-D simulations, is given in Figs. 8, 9, and 10. Figs. 8 and 9 compare the 2-D simulation form Sec. III, including all degradation sources, against a slice through the 3-D inviscid simulation discussed above. In both cases, the hohlraum symmetry axis is horizontal. Fig. 8 compares the material density at the time of peak implosion velocity (t = 22.53 ns) and at bang time (t = 22.83 ns) with the 2-D results in the left column and the 3-D results in the right column. Fig. 9 compares the flow speeds at the same two times. While the density distributions are broadly similar at both times in Fig. 8, except for the necessity of placing the fill tube on the symmetry axis in the 2-D simulations and the 3-D rupturing of the hot spot through the tent defect at bang time, the flow speeds in the forming hot spot are quite different beginning from the first time in Fig. 9. Comparing the flow speeds at the time of peak implosion velocity, the nearly turbulent flow in the 3-D simulation, already highlighted in the discussion of Fig. 6, contrasts markedly with the nearly laminar stagnating flow in the 2-D simulation. At bang time, again as described in the context of Fig. 6, the

smaller-scale, turbulent-like flow features are deemphasized relative to the larger-scale jet propagating along the simulation axis in the 2-D simulation and along the axis and out through the tent defect in the 3-D simulation. In the sense that both 2-D and 3-D simulations each now show flows with a similar range of scales, the large differences between 2-D and 3-D simulations at peak velocity appear to have substantially diminished by bang time.

Like Fig. 9, Fig. 10 compares a 2-D viscous simulation, analogous to the inviscid simulation in Fig. 9, against a slice through the 3-D viscous simulation. Whereas the inviscid simulations in Fig. 9 showed very different flow speeds at peak implosion velocity, with viscosity included, Fig. 10 shows that those differences are largely removed. That is, while added degrees of freedom are strongly excited in the 3-D simulation that cannot be represented in 2-D, these degrees of freedom are excited only at scales small enough that they are removed when physical viscosity is included. At bang time for these two simulations, the prominent difference is again at the large scale of the jet flowing though the center of the hot spot and out through the tent defect in 3-D. Even more so than in the inviscid cases, the smaller-scale flows have been deemphasized in the 3-D simulation, and the leading differences are in the orientation of the larger-scale jet. Fortuitously, when viscous effects are included, 2-D simulations appear to provide a serviceable model of the hot spot flow dynamics.

Lastly, for a quantitative comparison of the simulation results (2-D and 3-D) to the measured diagnostic signatures, the simulated results for several of the principle diagnostics are summarized in Table I. The table gives results for both 2-D and 3-D simulations, with and without viscosity, and the right most column lists the experimentally measured values. By construction of the x-ray source used to drive the simulations, the nuclear bang times for all cases are within the error bars of the data. The burn widths are within the error bars of the data

for all of the inviscid cases but are, interestingly, shorter than and just outslide of the error bars for the viscous cases. The equatorial x-ray image sizes (x-ray P_0) for the 2-D simulations both match the data within the error bars, while the 3-D simulation results are slightly lower than and, in the viscous case, just outside of the error bars. Note that the experimental x-ray image values (P_0 and P_2/P_0) listed in the table are for the ARIANE [55] instrument and not the usual hGXI instrument [56], since this is considered the more reliable diagnostic for this shot. Note also that the values reported for the 3-D simulations are the results of instantaneous ray trace post-processing of the 3-D results. These simulated images therefore do not include the time smearing due to the finite gate time of the real imaging instrument, as is included in the 2-D post-processing. This limitation is a necessity due to the very large scale of the 3-D simulations. At this time, compute capabilities are inadequate to accomplish the proper time smearing over many simulation time steps to model accurately this diagnostic signature. Nevertheless, the agreement with the instantaneous post-processing is encouragingly close to the data, and it can even be expected that, were it possible to include the correct time smearing in the post-processing, the simulated image sizes could increase to be even closer to the data. Bearing the same caveat in mind, the x-ray P_2/P_0 is within the error bars for the 3-D simulation but too low for the 2-D simulations, while the polar x-ray image size (x-ray M_0) is too low for both the 2-D and 3-D simulations although slightly closer for the 3-D results.

Turning to the nuclear data signatures in rows 7 – 13, the burn-weighted ion temperatures from all of the simulations are within the error bars of the data, although the 2-D inviscid simulation gives the closest match. The 4π-averaged DSR values from the 2-D simulations match the data within the error bars, but the 3-D simulations are somewhat too high. Like the simulated x-ray images, these 3-D DSR signatures can currently only be calculated from an

instantaneous PMC step at bang time. Given that the 3-D simulation results therefore lack the time smearing over the duration of the burn, as is included in the 2-D results, it is conceivable that post-processing the 3-D results to account for the time smearing could improve the agreement to the level seen with the 2-D simulations. In fact, comparing the instantaneous versus burn-averaged areal densities from the companion 1-D simulation shows that the instantaneous value exceeds the burn averaged value by ~ 13%. If the same proportionality is assumed to apply to the 3-D simulation, this suggests that the properly time-averaged DSR from the 3-D simulation should be ~ 6.1%, within the error bars of the data. Rigorously post-processing the 3-D simulations for these time integrated diagnostic signatures is a subject on ongoing work.

Given their full 3-D structure, the 3-D simulations can also be post-processed along the various lines of sight of the neutron spectrometers around the NIF target chamber. These results are summarized in rows 9 through 12. Like the 4π-averaged DSR value, the DSR values in each of these directions are high relative to the measured values; however, it is interesting that the spatial distribution of the DSR values appears to be qualitatively correct. That is, where the simulated DSR values are higher than average, the experimental values are also higher than average and vice versa. This suggests that, although the simulated compression in the 3-D simulation may be somewhat higher than the experimental value (albeit computed without the appropriate time averaging) the overall low-mode distribution or lumpiness of imploded mass is qualitatively correct.

The last line of Table 1 summarizes the primary neutron yield values from the simulations. As noted in Sec. III, the 2-D simulations give a neutron yield high by a factor of three relative to

the data for both viscous and inviscid simulations. The 3-D simulations reduce the yield by approximately a factor of two relative to 2-D such that the 3-D simulated yields are within ~ 50% of the experimental value. This appears to be related to the 3-D "venting" of the hot spot through the tent defect described above and the subsequent drop in hot spot temperature and density. Interestingly, for both 2-D and 3-D simulations, the viscous simulations show slightly higher yields than the inviscid simulations. The source of this difference in yield is still under investigation. Lastly, another implosion characteristic extracted from the nuclear data signatures is the inferred hot spot flow velocity based on shifts in the primary neutron spectrum peak and width. Although not shown in Table 1, the inferred hot spot flow velocities for N120321 are qualitatively consistent with the results of the 3-D simulation. These results are described in a companion paper [57].

V. CONCLUSIONS

This paper has summarized the results of detailed simulations of NIF shot N120321. N120321 is the highest compression shot yet fired on NIF and represents an important experiment for understanding the behavior of the high compression implosions necessary to achieve ignition at the NIF energy scale. The goal of this simulation study was to assess how well the standard simulation methodology compares to the data when updated to include the latest understanding of the degradation sources present in implosion experiments fired during the NIC. Without a thorough accounting for the effects now known to be present in NIC implosions and a detailed comparison of simulation results including these effects against the data, it is impossible to conclude that additional, yet undiscovered effects are not influencing implosion experiment results and that further investigations are necessary.

Given lingering uncertainties in the inputs to the simulation model, it is impossible to

conclude definitively that no other effects are present. It is conceivable that one of the effects modeled here (the surrogate tent and fill tube perturbations, the low-mode shape perturbations, or the pre-mixed ablator mass in the hot spot) could be overstated in the current simulations and masking another effect. For example, it is possible that hot electron pre-heat of the fuel, as mentioned above, could be a degradation mechanism that in some way offsets the performance degradation that here is accounted for by the hot spot mix mass. Instability growth that is a factor of two larger than modeled, and within the current uncertainty of HGR measurements, or significantly larger initial seeds for instability growth are other possibilities that could offset one of the effects included here within the uncertainties. Equally, it is possible that one of the effects modeled here, for example the tent perturbation, has been underrepresented and that increasing that perturbation could resolve the remaining yield deficit. Whether any of these scenarios can demonstrate the level of agreement with the data as shown in Table 1 remains to be shown, however. In this respect, it is important to bear in mind that an array of different observables are recorded for each implosion experiment. Any alternate simulation scenario must then show agreement across this range of observables at least as good as that shown in Table 1.

Nevertheless, the level of agreement between data and simulation described above is strongly suggestive that the leading order effects have been accounted for. While the agreement with the experimental data, as summarized in Table 1, is not perfect, it is significantly improved with respect to previous simulation studies. Arguably, it is sufficiently close in the case of the 3-D simulations to believe that the remaining discrepancies are within the limits of what can be expected given the ultimately incomplete knowledge of the implosion initial conditions. This is especially the case for such a highly nonlinear observable as the fusion yield. It is noteworthy

in this respect that a significant yield degradation is observed between 2-D and 3-D simulations, emphasizing the inherently 3-D character of the high convergence implosion studied here and necessary to understand for successful ignition on NIF.

ACKNOWLEGEMENTS

This work was performed under the auspices of the U.S. Department of Energy by Lawrence Livermore National Laboratory under Contract DE-AC52-07NA27344.

REFERENCES

[1] M. J. Edwards, P. K. Patel, J. D. Lindl, L. J. Atherton, s. H. Glenzer, S. W. Haan, J. D. Kilkenny, O. L. Landen, E. I. Moses, A. Nikroo, R. Petrasso, T. C. Sangster, P. T. Springer, S. Batha, R. Benedetti, L. Bernstein, R. Betti, D. L. Bleuel, T. R. Boehly, D. K. Bradley, J. A. Caggiano, D. A. Callahan, P. M. Celliers, C. J. Cerjan, K. C. Chen, D. S. Clark, G. W. Collins, E. L. dewald, L. Divol, S. Dixit, T. Deoppner, D. H. Edgell, J. E. Rai, M. Farrell, R. J. Fortner, J. Frenje, M. B. Gatu Johnson, E. Giraldez, V. Yu. Glebov, G. Grim, B. A. Hammel, A. V. Hamza, D. R. Harding, S. P. Hatchett, N. Hein, H. W. Herrmann, D. Hicks, D. E. Hinkel, M. Hoppe, W. W. Hsing, N. Izumi, B. Jacoby, O. S. Jones, D. Kalantar, R. Kauffman, J. L. Kline, J. P. Knauer, J. A. Koch, B. J. Kozioziemski, G. Kyrala, K. N. LaFortune, S. Le Pape, R. J. Leeper, R. Lerche, t. Ma, B. J. MacGaowan, A. J. MacKinnon, A. Macphee, E. R. Mapoles, M. M. Marinak, M. Mauldin, P. W. McKenty, M. Meezan, P. A. Michel, J. Milovich, J. D. Moody, M. Moran, D. H. Munro, C. L. Olson, K. Opachich, A. E. Pak, T. Parham, H.-S. Park, J. E. Ralph, S. P. Regan, B. Remington, H. Rinderknecht, H. F. Robey, M. Rosen, S. Ross, J. D. Salmonson, J. Sater, D. H. Schneider, F. H. Séguin, S. M. Sepke, D. A. Shaughnessy, V. A. Smalyuk, B. K. Spears, C. Stoeckl, W. Stoeffl, L. Suter, C. A. Thomas, R. Tommasini, R. P. Town, S. V. Weber, P. J. Webner, K. Widman, M. Wilke, D. C. Wilson, C. B. Yeamans, and A. Zylstra, Phys. Plasmas **20**, 070501 (2013).

[2] E. I. Moses, R. N. Boyd, B. A. Remington, C. J. Keane, and R. Al-Ayat, Phys. Plasmas **16** 041006 (2009).

[3] J. D. Lindl, P. A. Amendt, R. L. Berger, S. G. Glendinning, S. H. Glenzer, S. W. Haan, R. L. Kauffman, O. L. Landen, and L. J. Suter, Phys. Plasmas **11**, 339 (2004).

[4] S. Atzeni and J. Meyer-ter-Vehn *The Physics of Inertial Fusion* (Clarendon, Oxford, 2004).

[5] O. S. Jones, C. J. Cerjan, M. M. Marinak, J. L. Milovich, H. F. Robey, P. T. Springer, L. R. Benedetti, D. L. Bleuel, E. J. Bond, D. K. Bradley, D. A. Callahan, J. A. Caggiano, P. M. Celliers, D. S. Clark, S. M. Dixit, T. Döppner, R. J. Dylla-Spears, E. G. Dzentitis, D. R. Farley, S. M. Glenn, S. H. Glenzer, S. W. Haan, B. J. Haid, C. A. Haynam, D. G. Hicks, B. J. Kozioziemski, K. N. LaFortune, O. L. Landen, E. R. Mapoles, A. J. MacKinnon, J. M. McNaney, N. B. Meezan, P. A. Michel, J. D. Moody, M. J. Moran, D. H. Munro, M. V. Patel, T. G. Parham, J. D. Sater, S. M. Sepke, B. K. Spears, R. P. J. Town, S. V. Weber, K. Widmann, C. C. Widmayer, E. A. Williams, L. J. Atherton, M. J. Edwards, J. D. Lindl, B. J. MacGowan, L. J. Suter, R. E. Olson, H. W. Herrmann, J. L. Kline, G. A. Kyrala, D. C. Wilson, J. Frenje, T. R. Boehly, V. Glebov, J. P. Knauer, A. Nikroo, H. Wilkens, and J. D. Kilkenny, Phys. Plasmas **19**, 056315 (2012).

[6] D. S. Clark, D. E. Hinkel, D. C. Eder, O. S. Jones, S. W. Haan, B. A. Hammel, M. M. Marinak, J. L. Milovich, H. F. Robey, L. J. Suter, and R. P. J. Town, Phys. Plasmas **20**, 056318 (2014).

[7] M. M. Marinak, G. D. Kerbel, N. A. Gentile, O. Jones, D. Munro, S. Pollaine, T. R. Dittrich, and S. W. Haan, Phys. Plasmas **8**, 2275 (2001).

[8] V. N. Goncharov, T. C. Sangster, R. Betti, T. R. Boehly, M. J. Bonino, T. J. B. Collins, R. S. Craxton, J. A. Delettres, D. H. Edgell, R. Epstein, R. K. Follett, C. J. Forrest, D. H. Froula, V. Yu. Glebov, D. R. Harding, R. J. Henchen, S. X. Hu, I. V. Igumenshchev, R. A. V. Maximov, R. L. McCrory, P. W. McKenty, D. D. Meyerhofer, D. T. Michel, J. F. Myatt, R. Nora, P. B. Radha, S. P. Regan, W. Seka, W. T. Shmayda, R. W. Short, A. Shvydky, S. Skupsky, C. Stoeckl, B. Yaakobi, J. A. Frenji, M. Gatu-Johnson, r. D. Petrasso, and D. T. Casey, Phys. Plasmas **21**, 056315 (2014).

[9] T. R. Boehly, D. L. Brown, R. S. Craxton, R. L. Keck, J. P. Knauer, J. H. Kelly, T. J. Kessler, S. A. Kumpan, S. J. Loucks, S. A. Letzring, F. J. Marshall, R. L. McCrory, S. F. B. Morse, W. Seka, J. M. Soures, and C. P. Verdon, Opt. Commun. **133**, 495 (1997).

[10] O. A. Hurricane, D. A. Callahan, D. T. Casey, E. L. Dewald, T. R. Dittrich, T. Döppner, M. A. Barrios Garcia, D. E. Hinkel, L. F. Berzak Hopkins, P. Kervin, J. L. Kline, S. Le Pape, T. Ma, A. G. MacPhee, J. L. Milovich, J. Moody, A. E. Pak, P. K. Patel, H.-S. Park, B. A. Remington, H. F. Robey, J. D. Salmonson, P. T. Springer, R. Tommasini, L. R. Benedetti, J. A. Caggiano, P. Celliers, C. Cerjan, R. Dylla-Spears, D. Edgell, M. J. Edwards, D. Fittinghoff, G. P. Grim, N. Guler, N. Izumi, J. A. Frenje, M. Gatu Johnson, S. Haan, R. Hatarik, H. Herrmann, S. Khan, J. Knauer, B. J. Kozioziemski, A. L. Kritcher, G. Kyrala, S. A. Maclaren, F. E. Merrill, P. Michel, J. Ralph, J. S. Ross, J. R. Rygg, M. B. Schneider, B. K. Spears, K. Widmann, and C. B. Yeamans, Phys. Plasmas **21**, 056314 (2014).

[11] S. H. Glenzer, B. K. Spears, M. J. Edwards, E. T. Alger, R. L. Berger, D. L. Bleuel, D. K. Bradley, J. A. Caggiano, D. A. Callahan, C. Castro, D. T. Casey, C. Choate, D. S. Clark, C. J. Cerjan, G. W. Collins, E. L. Dewald, J. G. Di Nicola, P. Di Nicola, L. Divol, S. N. Dixit, T. Doppner, R. Dylla-Spears, E. G. Dzenitis, J. E. Fair, L. J. A. Frenje, M. Gatu-Johnson, E. Giraldez, V. Glebov, S. M. Glenn, S. W. Haan, B. A. Hammel, S. P. Hatchett II, C. A. Haynam, R. F. Heeter, G. M. Heestand, H. W. Herrmann, D. G. Hicks, D. M. Holunga, J. B. Horner, H. Huang, N. Izumi, O. S. Jones, D. H. Kalantar, J. D. Kilkenny, R. K. Kirkwood, J. L. Kline, J. P. Knauer, B. Kozioziemski, A. L. Kritcher, J. J. Kroll, G. A. Kyrala, K. N. LaFortune, O. L. Landen, D. W. Larson, R. J. Leeper, S. Le Pape, J. D. Lindl, T. Ma, A. J. Mackinnon, A. G. MacPhee, E. Mapoles, P. W. McKenty, N. B. Meezan, P. Michel, J. L. Milovich, J. D. Moody, A. S. Moore, M. Moran, K. A. Moreno, D. H. Munro, B. R. Nathan, A. Nikroo, R. E. Olson, C.

D. Orth, A. Pak, P. K. Patel, T. Parham, R. Petrasso, J. E. Ralph, H. Rinderknecht, S. P. Regan, H. F. Robey, J. S. Ross, J. D. Salmonson, C. Sangster, J. Sater, M. B. Schneider, F. H. Séguin, M. J. Shaw, M. J. Shoup, P. T. Springer, W. Stoeffl, L. J. Suter, C. A. Thomas, R. P. J. Town, C. Walters, S. V. Weber, P. J. Wegner, C. Widmayer, P. K. Whitman, K. Widmann, D. C. Wilson, B. M. Van Wonterghem, B. J. MacGowan, L. J. Atherton, and E. I. Moses, Plasma Phys. Control. Fusion **54**, 045013 (2012).

[12] O. L. Landen, J. Edwards, S. W. Haan, H. F. Robey, J. Milovich, B. K. Spears, S. V. Weber, D. S. Clark, J. D. Lindl, B. J. MacGowan, E. I. Moses, J. Atherton, P. A. Amendt, T. R. Boehly, D. K. Bradley, D. G. Braun, D. A. Callahan, P. M. Celliers, G. W. Collins, E. L. Dewald, L. Divol, J. A. Frenje, S. H. Glenzer, A. Hamza, B. A. Hammel, D. G. Hicks, N. Hoffman, N. Izumi, O. S. Jones, J. D. Kilkenny, R. K. Kirkwood, J. L. Kline, G. A. Kyrala, M. M. Marinak, N. Meezan, D. D. Meyerhofer, P. Michel, D. H. Munro, R. E. Olson, A. Nikroo, S. P. Regan, L. J. Suter, C. A. Thomas, and D. C. Wilson, Phys. Plasmas **18**, 051002 (2011).

[13] V. A. Smalyuk, L. J. Atherton, L. R. Benedetti, R. Bionta, D. Bleuel, E. Bond, D. K. Bradley, J. Caggiano, D. A. Callahan, D. T. Casey, P. M. Celliers, C. J. Cerjan, D. Clark, E. L. Dewald, S. N. Dixit, T. Döppner, D. H. Edgell, M. J. Edwards, J. Frenje, M. Gatu-Johnson, V. Y. Glebov, S. Glenn, S. H. Glenzer, G. Grim, S. W. Haan, B. A. Hammel, E. P. Hartouni, R. Hatarik, S. Hatchett, D. G. Hicks, W. W. Hsing, N. Izumi, O. S. Jones, M. H. Key, S. F. Khan, J. D. Kilkenny, J. L. Kline, J. Knauer, G. A. Kyrala, O. L. Landen, S. Le Pape, J. D. Lindl, T. Ma, B. J. MacGowan, A. J. Mackinnon, A. G. MacPhee, J. McNaney, N. B. Meezan, J. D. Moody, A. Moore, M. Moran, E. I. Moses, A. Pak, T. Parham, H.-S. Park, P. K. Patel, R. Petrasso, J. E. Ralph, S. P. Regan, B. A. Remington, H. F. Robey, J. S. Ross, B. K. Spears, P. T. Springer, L. J.

Suter, R. Tommasini, R. P. Town, S. V. Weber, and K. Widmann, Phys. Rev. Lett. **111**, 215001 (2013).

[14] W. H. Goldstein , *Workshop on the Science of Fusion Ignition on NIF*, San Ramon, CA, May 22 – 23, 2012.

[15] Lord Rayleigh, *Scientific Papers* (Cambridge University Press, Cambridge, England, 1900).

[16] G. I. Taylor, Proc. R. Soc. London, Ser. A **201**, 192 (1950).

[17] R. D. Richtmyer, Commun. Pure Appl. Math. **13**, 297 (1960).

[18] E. E. Meshkov, Fluid Dyn. **4**, 101 (1969).

[19] O. A. Hurricane, D. A. Callahan, D. T. Casey, P. M. Celliers, C. Cerjan, E. L. Dewald, T. R. Dittrich, T. Döppner, D. E. Hinkel, L. F. Berzak Hopkins, J. L. Kline, S. Le Pape, T. Ma, A. G. MacPhee, J. L. Milovich, A. Pak, H.-S. Park, P. K. Patel, B. A. Remington, J. D. Salmonson, P. T. Springer, and R. Tommasini, Nature **506**, 343 (2014).

[20] C. R. Weber, D. S. Clark, A. W. Cook, L. E. Busby, and H. F. Robey, Phys. Rev. E **89**, 053106 (2014).

[21] H. R. Robey, M. D. Rosen, D. Shvarts, B. Afeyan, D. S. Clark, E. L. Dewald, S. W. Haan, M. Hohenberger, A. L. Kritcher, W. Kruer, J. D. Lindl, M. M. Marinak, D. S. Montgomery, J. D. Moody, M. V. Patel, P. K. Patel, J. S. Ross, J. D. Salmonson, P. T. Springer, and C. R. Weber, Phys. Rev. Lett., *submitted* (2014).

[22] D. L. Bleuel, C. B. Yeamans, L. A. Bernstein, R. M. Bionta, J. A. Caggiano, D. T. Casey, G. W. Cooper, O. B. Drury, J. A. Frenje, C. A. Hagmann, R. Hatarik, J. P. Knauer, M. Gatu Johnson, K. M. Knittel, R. J. Leeper, J. M. McNaney, M. Moran, C. L. Ruiz, and D. H. G. Schneider, Rev. Sci. Insturm. **83** 10D313 (2012).

[23] R. P. J. Town, D. K. Bradley, A. Kritcher, O. S. Jones, J. R. Rygg, R. Tommasini, M. Barrios, L. R. Benedetti, L. F. Berzak Hopkins, P. M. Celliers, T. Döppner, E. L. Dewald, D. C. Eder, J. E. Field, S. M. Glenn, N. Izumi, S. W. Haan, S. F. Khan, J. L. Kline, G. A. Kyrala, T. Ma, J. L. Milovich, J. D. Moody, S. R. Nagel, A. Pak, J. L. Peterson, H. F. Robey, J. S. Ross, R. H. H. Scott, B. K. Spears, M. J. Edwards, J. D. Kilkenny, and O. L. Landen, Phys. Plasmas **21**, 056313 (2014).

[24] J. R. Rygg, O. S. Jones, J. E. Field, M. A. Barrios, L. R. Benedetti, G. W. Collins, D. C. Eder, M. J. Edwards, J. L. Kline, J. J. Kroll, O. L. Landen, T. Ma, A. Pak, J. L. Peterson, K. Raman, R. P. J. Town, and D. K. Bradley, Phys. Rev. Lett. **112**, 165001 (2014).

[25] A. L. Kritcher, R. Town, D. Bradley, D. Clark, B. Spears, O. Jones, S. Haan, P. T. Springer, J. Lindl, R. H. H. Scott, D. Callahan, M. J. Edwards, and O. L. Landen, Phys. Plasmas **21**, 042708 (2014).

[26] S. R. Nagel, *et al*., *in preparation* (2014).

[27] B. A. Hammel, H. A. Scott, S. P. Regan, C. Cerjan, D. S. Clark, M. J. Edwards, R. Epstein, S. H. Glenzer, S. W. Haan, N. Izumi, J. A. Koch, G. A. Kyrala, O. L. Landen, S. H. Langer, K. Peterson, V. A. Smalyuk, L. J. Suter, and D. C. Wilson, Phys. Plasmas **18**, 056310 (2011).

[28] S. W. Haan, J. D. Lindl, D. A. Callahan, D. S. Clark, J. D. Salmonson, B. A. Hammel, L. J. Atherton, R. C. Cook, M. J. Edwards, S. Glenzer, A. V. Hamza, S. P. Hatchett, M. C. Herrmann, D. E. Hinkel, D. D. Ho, H. Huang, O. S. Jones, J. Kline, G. Kyrala, O. L. Landen, B. J. MacGowan, M. M. Marinak, D. D. Meyerhofer, J. L. Milovich, K. A. Moreno, E. I. Moses, D. H. Munro, A. Nikroo, R. E. Olson, K. Peterson, S. M. Pollaine, J. E. Ralph, H. F. Robey, B. K. Spears, P. T. Springer, L. J. Suter, C. A. Thomas, R. P. Town, R. Vesey, S. V. Weber, H. L. Wilkens, and D. C. Wilson, Phys. Plasmas **18**, 051001 (2011).

[29] S. P. Regan, R. Epstein, B. A. Hammel, L. J. Suter, H. A. Scott, M. A. Barrios, D. K. Bradley, D. A. Callahan, C. Cerjan, G. W. Collins, S. N. Dixit, T. Döppner, M. J. Edwards, D. R. Farely, K. B. Fournier, S. Glenn, S. H. Glenzer, I. E. Golovkin, S. W. Haan, A. Hamza, D. G. Hicks, N. Izumi, O. S. Jones, J. D. Kilkenny, J. L, Kline, G. A. Kyrala, O. L. Landen, T. Ma, J. J. MacFarlane, A. J. MacKinnon, R. C. Mancini, R. L. McCrory, N. B. Meezan, D. D. Meyerhofer, A. Nikroo, H.-S. Park, J. Ralph, B. A. Remington, T. C. Sangster, V. A. Smalyuk, R. T. Springer, and R. P. J. Town, Phys. Rev. Lett. **111**, 045001 (2013).

[30] D. E. Hinkel, D. S. Clark, D. C. Eder, and O. S. Jones, Bull Am. Phys. Soc. **57**, 240 (2012).

[31] T. Ma, P. K. Patel, N. Izumi, P. T. springer, M. H. Key, L. J. Atherton, L. R. Benedetti, D. K. Bradley, D. A. Callahan, P. M. Celliers, C. J. Cerjan, D. S. Clark, E. L. Dewald, S. N. Dixit, T. Döppner, D. H. Edgell, R. Epstein, s. Glenn, G. Grim, S. W. Haan, B. A. Hammel, D. Hicks, W. W. Hsing, O. S. Jones, S. F. Khan, J. D. Kilkenny, J. L. Kline, G. A. Kyrala, O. L. Landen, S. Le Pape, B. J. MacGowna, A. J. Mackinnon, A. G. MacPhee, N. B. Meezan, J. D. Moody, A. Pak, T. Parham, H.-S. Park, J. E. Ralph, s. P. Regan, B. A. Remington, H. F. Robey, J. S. Ross, B. K. Spears, V. Smalyuk, L. J. Suter, R. Tommasini, R. P. Town, S. V. Weber, J. D. Lindl, M. J. Edwards, S. H. Glenzer, and E. I. Moses, Phys. Rev. Lett. **111**, 085004 (2013).

[32] H. F. Robey, T. R. Boehly, P. M. Celliers, J. H. Eggert, D. Hicks, R. F. Smith, R. Collins, M. W. Bowers, K. G. Krauter, P. S. Datte, D. H. Munro, J. L. Milovich, O. S. Jones, P. A. Michel, C. A. Thomas, R. E. Olson, S. Pollaine, R. P. J. Town, S. Haan, D. Callahan, D. Clark, J. Edwards, J. L. Kline, S. Dixit, M. B. Schneider, E. L. Dewald, K. Widmann, J. D. Moody, T. Döppner, H. B. Radousky, A. Throop, D. Kalantar, P. DiNicola, A. Nikroo, J. J. Kroll, A. V. Hamza, J. B. Horner, S. D. Bhandarkar, E. Dzenitis, E. Alger, E. Giraldez, C. Castro, K. Moreno, C. Haynam, K. N. LaFortune, C. Widmayer, M. Shaw, K. Jancaitis, T. Parham, D. M. Holunga, C.

F. Walters, B. Haid, E. R. Mapoles, J. Sater, C. R. Gibson, T. Malsbury, J. Fair, D. Trummer, K. R. Coffee, B. Burr, L. V. Berzins, C. Choate, S. J. Brereton, S. Azevedo, H. Chandrasekaran, D. C. Eder, N. D. Masters, A. C. Fisher, P. A. Sterne, B. K. Young, O. L. Landen, B. M. Van Wonterghem, B. J. MacGowan, J. Atherton, J. D. Lindl, D. D. Meyerhofer, and E. Moses, Phys. Plasmas **19**, 042706 (2012).

[33] D. G. Hicks, , N. B. Meezan, E. L. Dewald, A. J. Mackinnon, D. A. Callahan, T. Döppner, L. R. Benedetti, D. K. Bradley, P. M. Celliers, D. S. Clark, S. N. Dixit, E. G. Dzenitis, J. E. Eggert, D. R. Farley, S. M. Glenn, S. H. Glenzer, A. V. Hamza, R. F. Heeter, J. P. Holder, N. Izumi, D. H. Kalantar, S. F. Khan, J. J. Kroll, T. Ma, A. G. MacPhee, J. M. McNaney, J. D. Moody, M. J. Moran, B. R. Nathan, K. P. Opachich, R. R. Prasad, J. E. Ralph, H. F. Robey, J. R. Rygg, J. D. Salmonson, M. B. Schneider, N. Simanovskaia, B. K. Spears, R. Tommasini, K. Widmann, G. W. Collins, O. L. Landen, J. D. Kilkenny, W. W. Hsing, B. J. MacGowan, L. J. Atherton, M. J. Edwards, R. E. Olson, J. A Frenje, R. D. Petrasso, H. G. Rinderknecht, A. B. Zylstra, J. L Kline, G. A. Kyrala, and A. Nikroo, Phys. Plasmas **19**, 122702 (2012).

[34] J. A. Frenje, D. T. Casey, C. K. Li, F. H. Séguin, R. D. Petrasso, V. Yu Glebov, P. B. Radha, T. C. Sangster, D. D. Meyerhofer, S. P. Hatchett, S. W. Haan, C. J. Cerjan, O. L. Landen, K. A. Fletcher, and R. J. Leeper, Phys. Plasmas **17**, 056311 (2010).

[35] S. A. MacLaren, M. B. Schneider, K. Widmann, J. H. Hammer, B. E. Yoxall, J. D. Moody, P. M. Bell, L. R. Benedetti, K. K. Bradley, and M. J. Edwards, Phys. Rev. Lett. **112**, 105003 (2014).

[36] K. S. Raman, V. A. Smalyuk, D. T. Casey, S. W. Haan, D. E. Hoover, O. A. Hurricane, J. J. Kroll, A. Nikroo, J. L. Peterson, B. A. Remington, H. F. Robey, D. S. Clark, B. A. Hammel, O. L. Landen, M. M. Marinak, D. H. Munro, K. J. Peterson, and J. Salmonson, Phys. Plasmas **21**, 072710 (2014).

[37] D. T. Casey, V. A. Smalyuk, K. S. Raman, J. L. Peterson, L. Berzak Hopkins, D. A. Callahan, D. S. Clark, E. L. Dewald, T. R. Dittrich, S. W. Haan, D. E. Hinkel, D. Hoover, O. A. Hurricane, J. J. Kroll, O. L. Landen, A. S. Moore, A. Nikroo, H.-S. Park, B. A. Remington, H. F. Robey, J. R. Rygg, J. D. Salmonson, R. Tommasini, and K. Widmann, Phys. Rev. E **90**, 011102(R) (2014).

[38] V. A. Smalyuk, M. Barrios, J. A. Caggiano, D. T. Casey, C. J. Cerjan, D. S. Clark, M. J. Edwards, J. A. Frenje, M. Gatu-Johnson, V. Y. Glebov, G. Grim, S. W. Haan, B. A. Hammel, A. Hamza, D. E. Hoover, W. W. Hsing, O. Hurricane, J. D. Kilkenny, J. L. Kline, J. P. Knauer, J. Kroll, O. L. Landen, J. D. Lindl, T. Ma, J. M. McNaney, M. Mintz, A. Moore, A. Nikroo, T. Parham, J. L. Peterson, R. Petrasso, L. Pickworth, J. E. Pino, K. Raman, S. P. Regan, B. A. Remington, H. F. Robey, D. P. Rowley, D. B. Sayre, R. E. Tipton, S. V. Weber, K. Widmann, D. C. Wilson, and C. B. Yeamans, Phys. Plasmas **21**, 056301 (2014).

[39] B. A. Hammel, *private communication* (2014).

[40] S. W. Haan, L. Berzak Hopkins, D. S. Clark, D. Eder, B. A. Hammel, A. Hamza, D. Ho, O. S. Jones, A. Kritcher, K. LaFortune, B. J. MacGowan, N. B. Meezan, J. Milovich, J. L. Peterson, H. F. Robey, J. D. Salmonson, B. K. Spears, R. P. Town, J. L. Kline, D. C. Wilson, A. N. Simakov, S. A. Yi, A. Nikroo, H. Huang, and D. Hoover, Bull. Am. Phys. Soc. **58**, 155 (2013).

[41] D. S. Clark, S. W. Haan, and J. D. Salmonson, Phys. Plasmas **15**, 056305 (2008).

[42] M. M. Marinak, B. A. Remington, S. V. Weber, R. E. Tipton, S. W. Haan, K. S. Budil, O. L. Landen, J. D. Kilkenny, and R. Wallace, Phys. Rev. Lett. **75**, 3677 (1995).

[43] M. M. Marinak, R. E. Tipton, O. L. Landen, T. J. Murphy, P. Amendt, S. W. Haan, S. P. Hatchett, C. J. Keane, R. McEachern, and R. Wallace, Phys. Plasmas **3**, 2070 (1996).

[44] M. M. Marinak, S. W. Haan, T. R. Dittrich, R. E. Tipton and G. B. Zimmerman, Phys. Plasmas **5**, 1125 (1998).

[45] M. M. Marinak, S. G. Glendinning, R. J. Wallace, B. A. Remington, K. S. Budil, S. W. Haan, R. E. Tipton, and J. D. Kilkenny, Phys. Rev. Lett. **80**, 4426 (1998).

[46] B. A. Hammel, S. W. Haan, D. S. Clark, M. J. Edwards, S. H. Langer, M. M. Marinak, M. V. Patel, J. D. Salmonson, and H. A. Scott, High Energy Density Physics **6**, 171 (2010).

[47] D. S. Clark, S. W. Haan, A. W. Cook, M. J. Edwards, B. A. Hammel, J. M. Koning, and M. M. Marinak, Phys. Plasmas **18**, 082701 (2011).

[48] S. W. Haan, P. A. Amendt, T. R. Dittrich, B. A. Hammel, S. P. Hatchett, M. C. Herrmann, O. A. Hurricane, O. S. Jones, J. D. Lindl, M. M. Marinak, D. Munro, S. M. Pollaine, J. D. Salmonson, G. L. Strobel, and L. J. Suter, Nucl. Fusion **44**, S171 (2004).

[49] M. Gittings, R. Weaver, M. Clover, T. Betlach, N. Byrne, R. Coker, E. Dendy, R. Hueckstaedt, K. New, W. R. Oakes, D. Ranta, and R. Stefan, Comput. Sci. Discovery **1**, 015005 (2008).

[50] B. M. Haines, F. F. Grinstein, and J. R. Fincke, Phys. Rev. E **89**, 053302 (2014).

[51] H. Huang, R. B. Stephens, J. B. Gibson, and I. Valmainski, Fusion Sci. Technology **49**, 642 (2006).

[52] A. Q. L. Nguyen, S. A. eddinger, H. Huang, M. A. Johnson, Y. T. Lee, R. C. Montesanti, K. A. Moreno, and M. E. Schoff, Fusion Sci. Technology **55**, 399 (2009).

[53] B. J. Kozioziemski, E. R. Mapoles, J. D. Sater, A. A. Chernov, J. D. Moody, J. B. Lugten, and M. A. Johnson, Fusion Sci. Technology **59**, 14 (2011).

[54] Y. T. Lee and R. M. More, Phys Fluids **27**, 1273 (1984).

[55] P. M. Bell, D. K. Bradley, J. D. Kilkenny, A. Conder, C. Cerjan, C. Hagmann, D. Hey, N. Izumi, J. Moody, A. Teruya, J. Celeste, J. Kimbrough, H. Khater, M. J. Eckart, and J. Ayers, Rev. Sci. Instrum. **81**, 10E540 (2010).

[56] S. Glenn, J. Koch, D. K. Bradley, N. Izumi, P. Bell, J. Holder, G. Stone, R. Prasad, A. MacKinnon, P. Springer, O. L. Landen and G. Kyrala, Rev. Sci. Instrum. **81**, 10E539 (2010).

[57] C. R. Weber, *in preparation* (2014).

Table 1. Summary of simulated outputs for N120321: 2-D and 3-D, viscous and inviscid simulations.

	2-D		3-D		
	invisc.	visc.	invisc.	visc.	expt.
bang time (ns)	22.85	22.83	22.81	22.83	22.83±0.04
burn width (ps)	130	109	127	105	136±24
x-ray P_0 (μm)	20.9	—	18.8*	18.4*	20.1±1.4¶
x-ray P_2/P_0	0.01	—	0.07*	0.07*	0.08±0.03¶
x-ray M_0 (μm)	16.4	—	18.0*	17.2*	22.7±2.7
x-ray M_2/M_0	—	—	- 0.08*	- 0.07*	0.16±0.02
T_{ion} (keV)	2.8	2.9	2.5	2.5	2.7±0.2
4π DSR (%)	6.3	6.2	6.9	7.1	6.0±0.5
NIS DSR (%)	—	—	7.0	7.3	6.3±0.5
SpecA DSR (%)	—	—	7.7	8.0	6.7±0.5
SpecE DSR (%)	—	—	6.4	6.6	5.1±0.4
MRS DSR (%)	—	—	7.0	7.3	7.0±0.4
neutrons (13 – 15 MeV)	1.5×10^{15}	1.6×10^{15}	6.0×10^{14}	7.2×10^{14}	$4.1\pm0.1\times10^{14}$

* from instantaneous ray trace at bang time
§ from single PMC step at bang time
¶ value from ARIANE instrument

FIGURE CAPTIONS

Fig. 1. (Color online) Summary of progress in NIC implosion performance plotted in the plane of neutron yield versus areal density. The blue symbols represent low foot shots fired during the NIC, and the green symbols represent high foot shots fired subsequent to the NIC. The dashed lines are contours of yield amplification due to α-particle self-heating as predicted from simulations. Shot N120321 reached the highest DT fuel areal density of any shot so far fired on NIF but showed negligible α-particle self-heating.

Fig. 2. (Color online) Comparison of imploded configurations at bang time from 2-D simulations including individual sources of performance degradation. In each panel, the upper half shows material density on the same color scale given at the right, and the lower half shows material region, the blue regions representing DT gas and ice and the remaining colors representing the various layers of doped plastic ablator. The red contour line in each panel represents the boundary between the low-density, high-temperature hot stop and the cold fuel according to a standard definition. From left to right and top to bottom the panels show the 1-D unperturbed implosion, the effect of including 200 ng of ablator mix in the hot spot, the effect of P_2 and P_4 x-ray flux asymmetries, the effect of the surrogate fill tube perturbation, the effect of the surrogate tent perturbation, and finally the effect of the measured surface roughness on the DT ice inner surface and outer ablator surface. Surface roughnesses according to specifications are also included on the interior surfaces in this last case but could not be measured directly.

Fig. 3. (Color online) Comparison of imploded configurations at bang time from 2-D simulations in which the performance degradation sources shown in Fig. 2 are added

incrementally running from left to right and top to bottom. The first two panels repeat from Fig. 2 showing the unperturbed 1-D simulation, and the effect of including ablator mix in the hot spot.

Fig. 4. (Color online) Summary of 2-D simulated diagnostic values for neutron yield, ion temperature, DSR, and x-ray image size as a function of perturbation from 1-D. In each panel, the experimentally measured value with its error bar is represented by the pink band. The blue bars represent the simulated value for each observable when the perturbations are included in individually, as in Fig. 2, and the red bars represent the simulated values when the perturbations are added incrementally, as in Fig. 3. When all degradation sources are included, as in the right-most red bar in each panel, all of the simulated observables are within the error bars of the data except for the yield.

Fig. 5. (Color online) Renderings of the DT ice-gas interface (a) and outer ablator surface (b) used as initial conditions for the 3-D HYDRA simulation of N120321. In each, the color scale shows the deviation from the mean radius of the interface. Measured low mode and high mode surface finish data is incorporated in generating each surface. A large 3-D ice groove is apparent in (a), while the dark blue bands encircling the poles in (b) are due to the surrogate tent perturbation model.

Fig. 6. (Color online) Snapshots of the state of the 3-D simulation of N120321 between the time of peak implosion velocity (22.53 ns) and the final time from the simulation (22.96 ns). In each snapshot, the outer green boundary is the interface between the DT fuel and the plastic ablator. The large spike-like perturbations on this interface are due to feed through of ablation front instability growth seeded by localized defects in the ablator surface. The cutaway surfaces

in each snapshot are colored with the fluid speed on the left for each time and the material density on the right. The length scale and density color scale change from snapshot to snapshot, but the velocity color scale is constant. The prominent perturbations caused by the surrogate tent perturbation and the fill tube are apparent through the first three times. The low-mode flux asymmetries also lead to a highly prolate shape to the implosion at bang time (22.83 ns). Also apparent at bang time and at the final time (22.96 ns) is the high speed jet of hot spot material "venting" to the upper left through the tent defect.

Fig. 7. (Color online) Comparison of inviscid and viscous 3-D simulations of N120321. The rows shows renderings analogous to Fig. 6 at the time of peak implosion velocity and bang time, and the columns compare the inviscid results (left) to the viscous results (right). The right column repeats from Fig. 6. The strong viscous dissipation entirely removes the small scale structures present in the low-density, nascent hot spot at peak velocity. At bang time, while the smaller-scale features have again been dissipated, the larger-scale jet of hot spot material "venting" through the tent defect persists. Viscosity also weakly damps the growth of the spike-like defects on the fuel ablator interface and slightly reduces the peak density.

Fig. 8. (Color online) Comparison of material density in a 2-D inviscid simulation of N120321 (left column) versus the 3-D inviscid simulation (right column). The upper row compares the results at peak implosion velocity, and the bottom row compares the results at bang time. The black contour denotes the fuel-ablator interface. The defects caused by the surrogate tent perturbation and the surrogate fill tube perturbation are apparent, although in the 2-D simulation the fill tube must be placed on the 2-D symmetry axis which is not the correct orientation with respect to the tent and low-mode flux asymmetries. Qualitatively, the density distributions are very similar.

Fig. 9. (Color online) Comparison of 2-D versus 3-D fluid speeds for the same simulations and times as shown in Fig. 8. At the time of peak velocity (upper row), a much more structured, near-turbulent flow field develops in 3-D as compared to 2-D. By bang time, the finer-scale structures in the 3-D flow have become less prominent, and the flow is dominated by a jet directed to the lower right through the tent defect. Qualitatively, this structure is more similar to the 2-D simulation, although its orientation through the tent defect is a uniquely 3-D effect.

Fig. 10. (Color online) Comparison of 2-D versus 3-D fluid speeds in simulations analogous to Fig. 9 but including viscosity. The fine scale structures in the 3-D inviscid simulation at peak velocity in Fig. 9 have been completely dissipated such that the 2-D and 3-D simulation results, serendipitously, look very similar at both early and late times. The orientation of the axial jet in the 3-D simulation through the tent defect is again a distinctly 3-D effect.

Fig. 1.

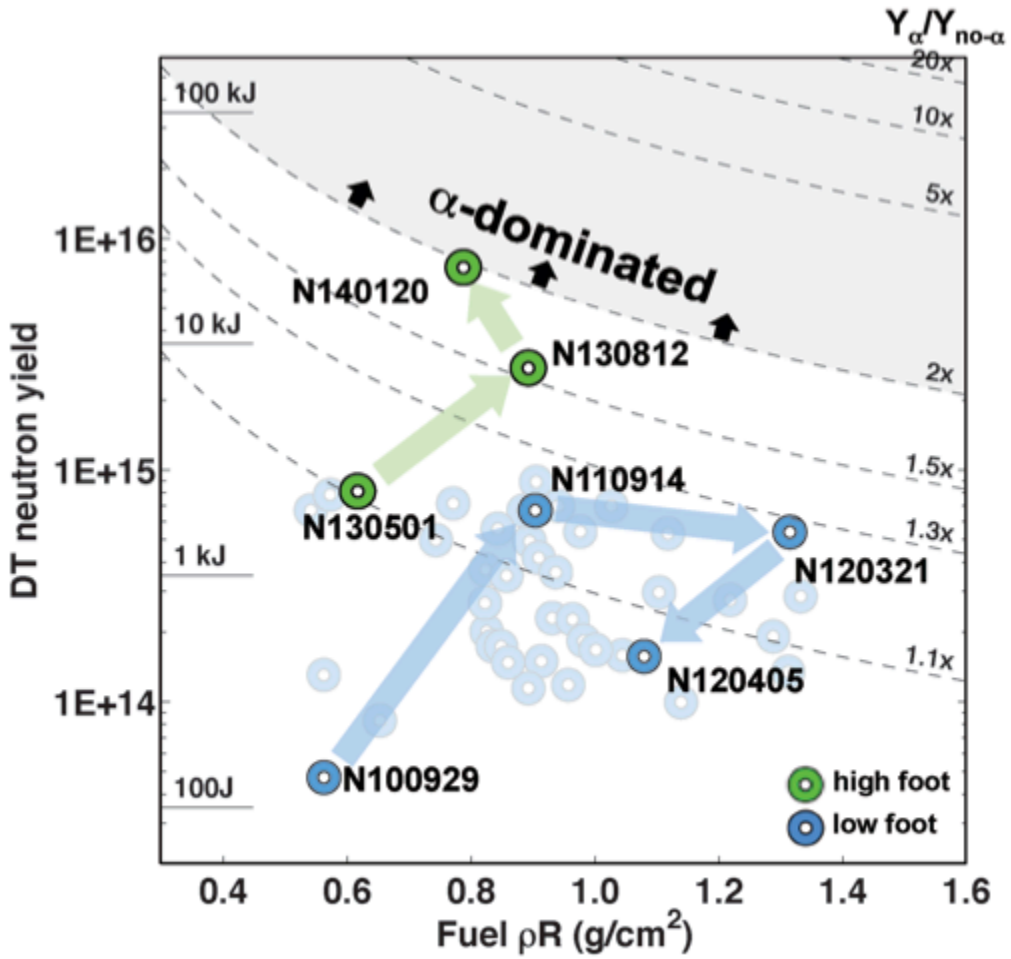
$Y_\alpha/Y_{no\text{-}\alpha}$
20x
10x
5x
2x
1.5x
1.3x
1.1x
100 kJ
10 kJ
1 kJ
100J
α-dominated
N140120
N130812
N130501
N110914
N120321
N120405
N100929
high foot
low foot
1E+16
1E+15
1E+14
DT neutron yield
0.4
0.6
0.8
1.0
1.2
1.4
1.6
Fuel ρR (g/cm^2)

Fig. 2.

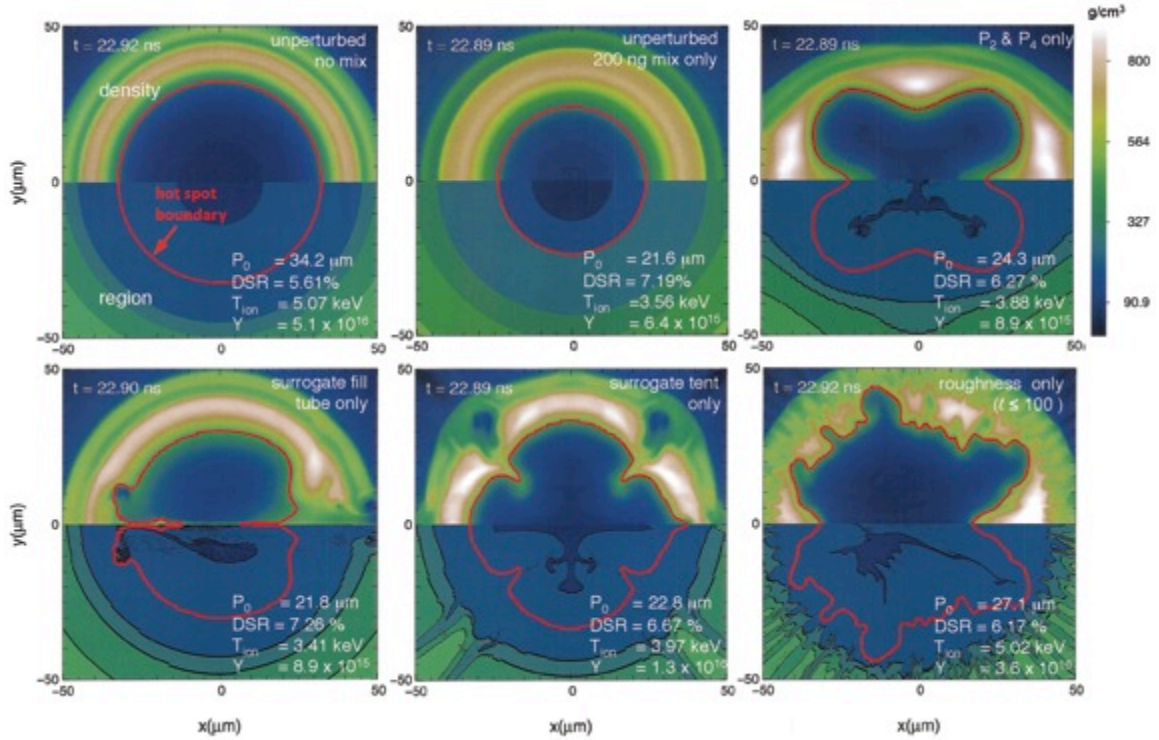
t = 22.92 ns
unperturbed
no mix
density
hot spot
boundary
region
P0 = 34.2 μm
DSR = 5.61%
Tion = 5.07 keV
Y = 5.1 x 10^16
t = 22.89 ns
unperturbed
200 ng mix only
P0 = 21.6 μm
DSR = 7.19%
Tion = 3.56 keV
Y = 6.4 x 10^15
t = 22.89 ns
P2 & P4 only
P0 = 24.3 μm
DSR = 6.27 %
Tion = 3.88 keV
Y = 8.9 x 10^15
g/cm3
800
564
327
90.9
t = 22.90 ns
surrogate fill
tube only
P0 = 21.8 μm
DSR = 7.26 %
Tion = 3.41 keV
Y = 8.9 x 10^15
t = 22.89 ns
surrogate tent
only
P0 = 22.8 μm
DSR = 6.67 %
Tion = 3.97 keV
Y = 1.3 x 10^16
t = 22.92 ns
roughness only
(ℓ ≤ 100)
P0 = 27.1 μm
DSR = 6.17 %
Tion = 5.02 keV
Y = 3.6 x 10^15
y(μm)
x(μm)
50
0
−50

Fig. 3.

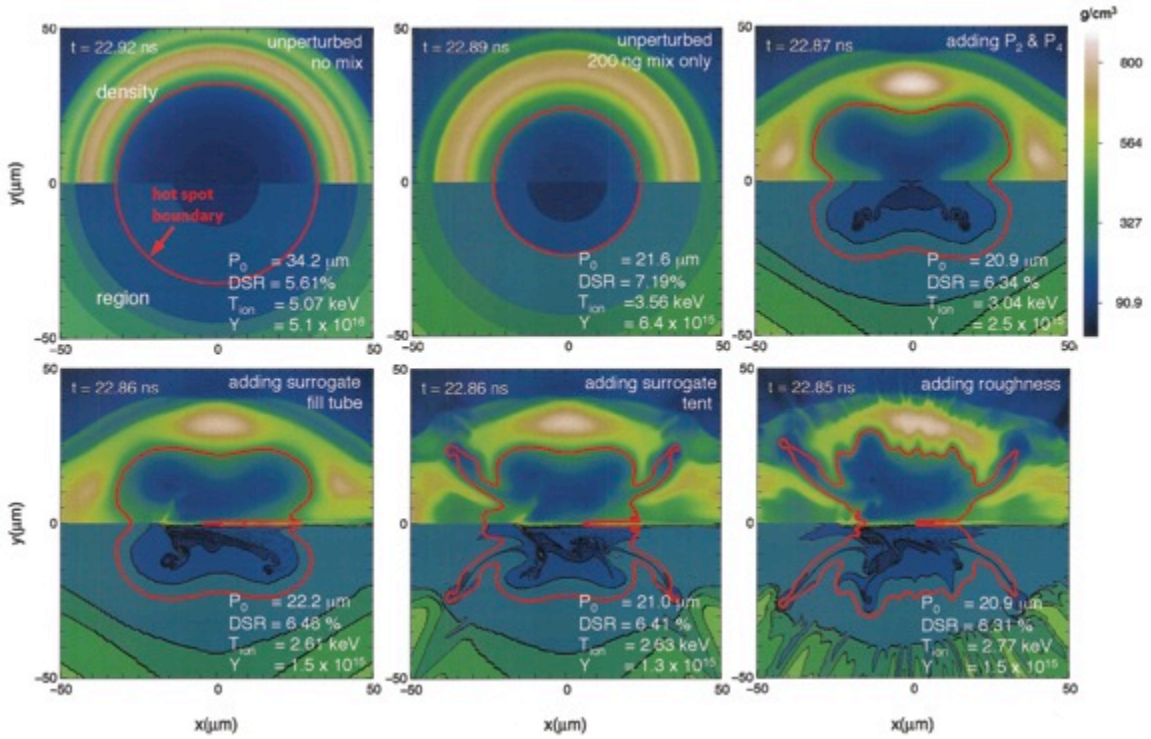
t = 22.92 ns
unperturbed
no mix
density
hot spot
boundary
region
P0 = 34.2 μm
DSR = 5.61%
Tion = 5.07 keV
Y = 5.1 x 10^16
t = 22.89 ns
unperturbed
200 ng mix only
P0 = 21.6 μm
DSR = 7.19%
Tion =3.56 keV
Y = 6.4 x 10^15
t = 22.87 ns
adding P2 & P4
P0 = 20.9 μm
DSR = 6.34 %
Tion = 3.04 keV
Y = 2.5 x 10^15
g/cm3
600
564
327
90.9
t = 22.86 ns
adding surrogate
fill tube
P0 = 22.2 μm
DSR = 6.48 %
Tion = 2.61 keV
Y = 1.5 x 10^15
t = 22.86 ns
adding surrogate
tent
P0 = 21.0 μm
DSR = 6.41 %
Tion = 2.63 keV
Y = 1.3 x 10^15
t = 22.85 ns
adding roughness
P0 = 20.9 μm
DSR = 6.31 %
Tion = 2.77 keV
Y = 1.5 x 10^15
y(μm)
x(μm)
50
0
-50

Fig. 4.

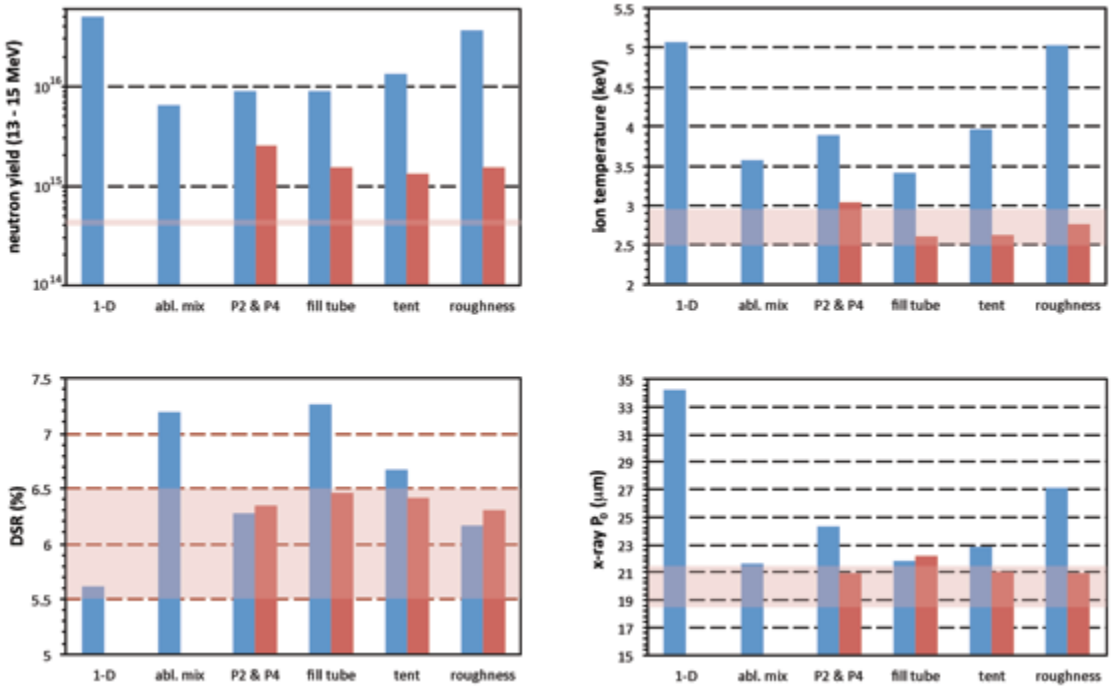
neutron yield (13 - 15 MeV)
10^{16}
10^{15}
10^{14}
1-D
abl. mix
P2 & P4
fill tube
tent
roughness
ion temperature (keV)
5.5
5
4.5
4
3.5
3
2.5
2
DSR (%)
7.5
7
6.5
6
5.5
5
x-ray P_0 (μm)
35
33
31
29
27
25
23
21
19
17
15

Fig. 5.

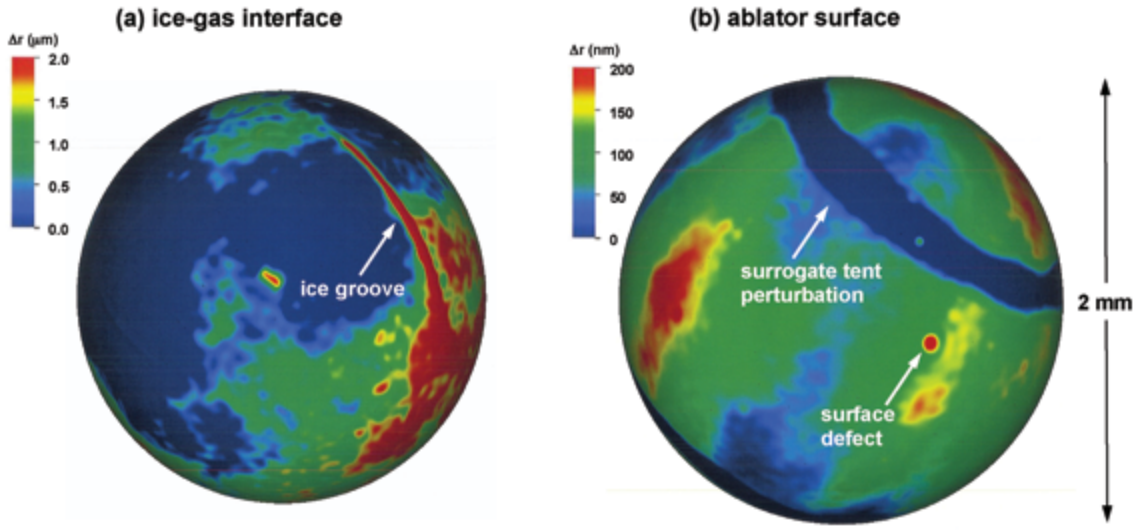
(a) ice-gas interface
Δr (μm)
2.0
1.5
1.0
0.5
0.0
ice groove
(b) ablator surface
Δr (nm)
200
150
100
50
0
surrogate tent
perturbation
surface
defect
2 mm

Fig. 6.

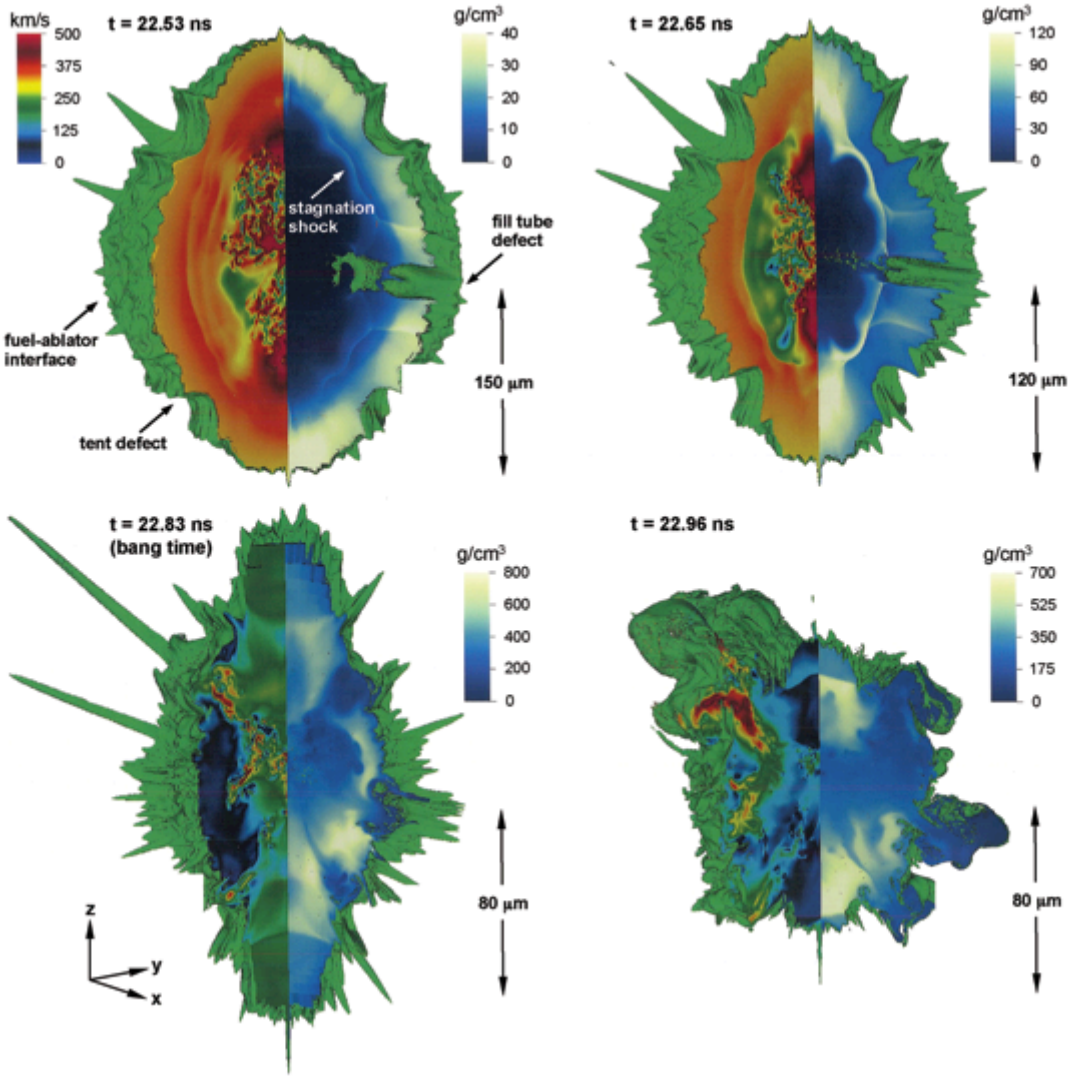
km/s
500
375
250
125
0
t = 22.53 ns
g/cm3
40
30
20
10
0
stagnation shock
fill tube defect
fuel-ablator interface
tent defect
150 μm
t = 22.65 ns
g/cm3
120
90
60
30
0
120 μm
t = 22.83 ns (bang time)
g/cm3
800
600
400
200
0
80 μm
z
y
x
t = 22.96 ns
g/cm3
700
525
350
175
0
80 μm

Fig. 7.

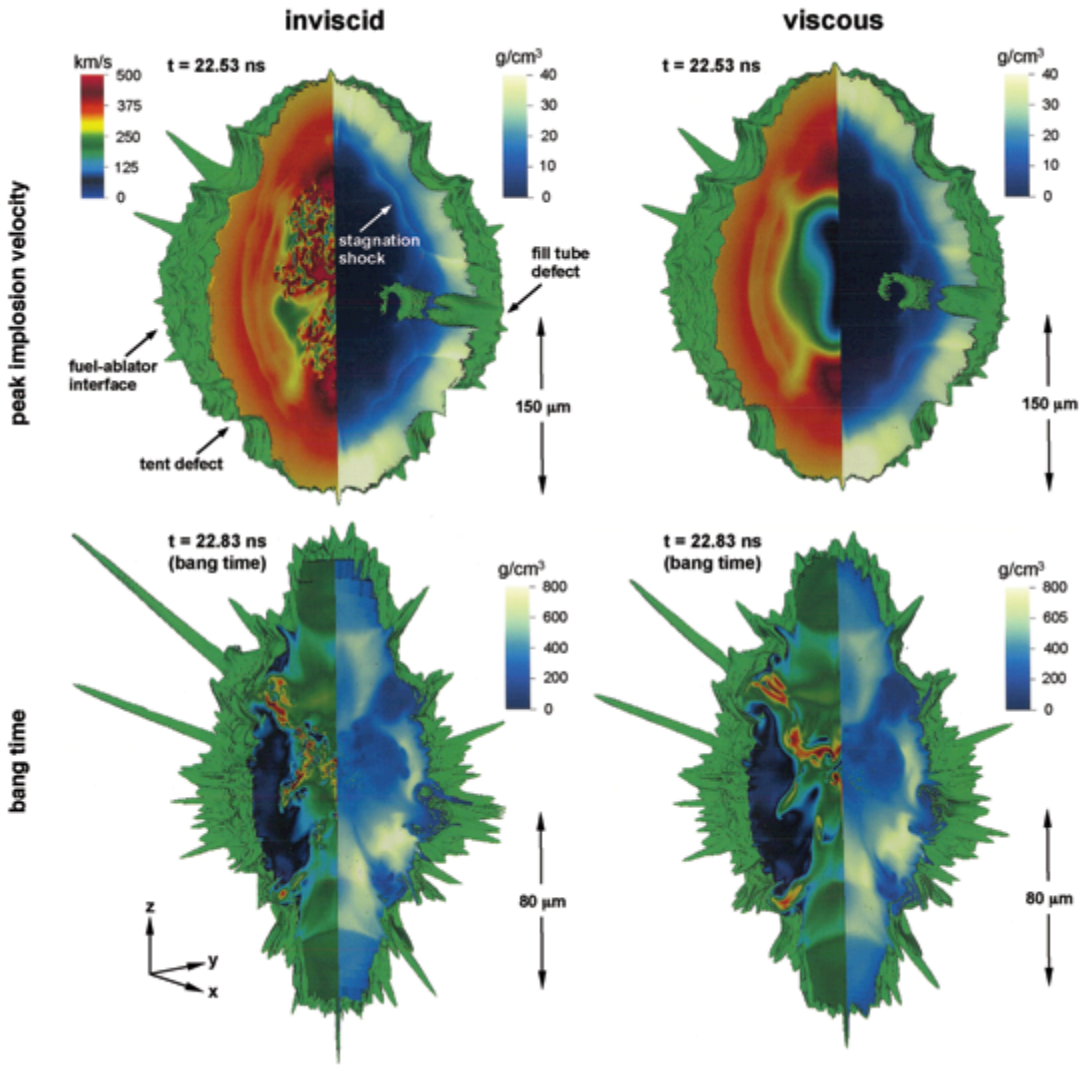
inviscid
viscous
peak implosion velocity
bang time
km/s
500
375
250
125
0
t = 22.53 ns
g/cm3
40
30
20
10
0
stagnation shock
fill tube defect
fuel-ablator interface
tent defect
150 μm
t = 22.83 ns (bang time)
800
600
400
200
605
80 μm
z
y
x

Fig. 8.

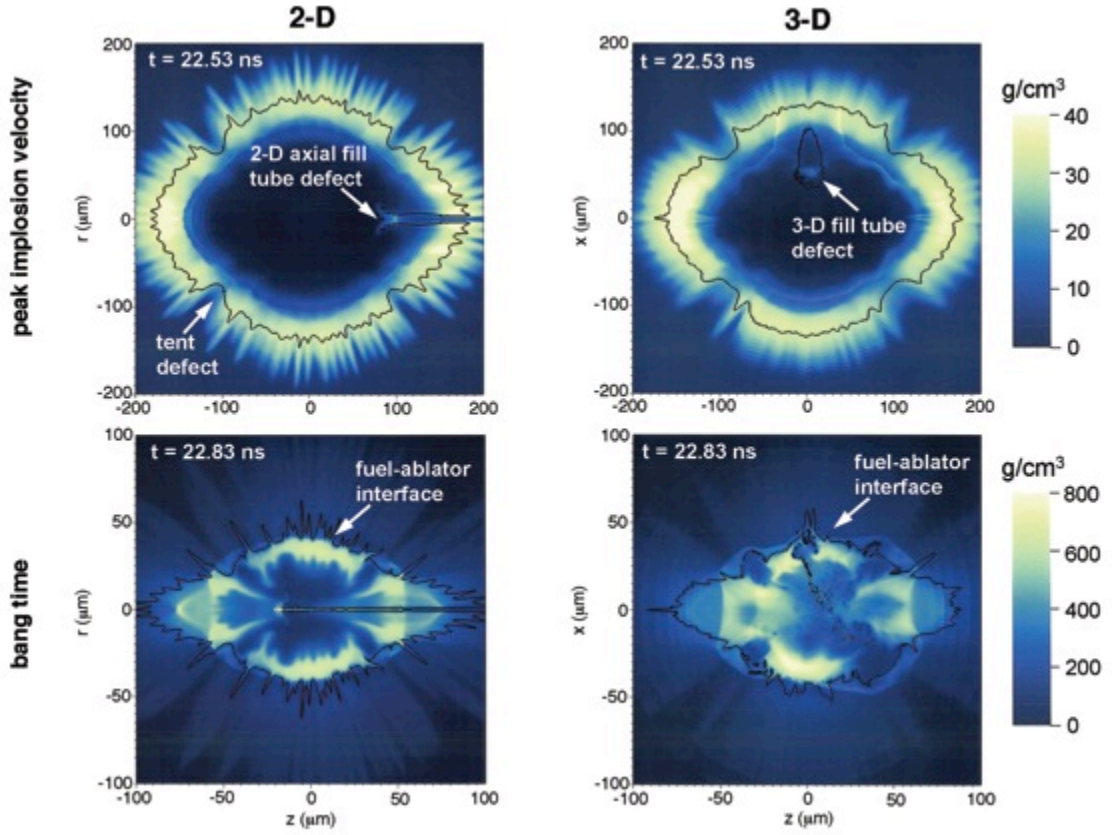
2-D
3-D
peak implosion velocity
bang time
t = 22.53 ns
2-D axial fill tube defect
tent defect
3-D fill tube defect
t = 22.83 ns
fuel-ablator interface
r (μm)
x (μm)
z (μm)
g/cm3
40
30
20
10
0
800
600
400
200
0

Fig. 9.

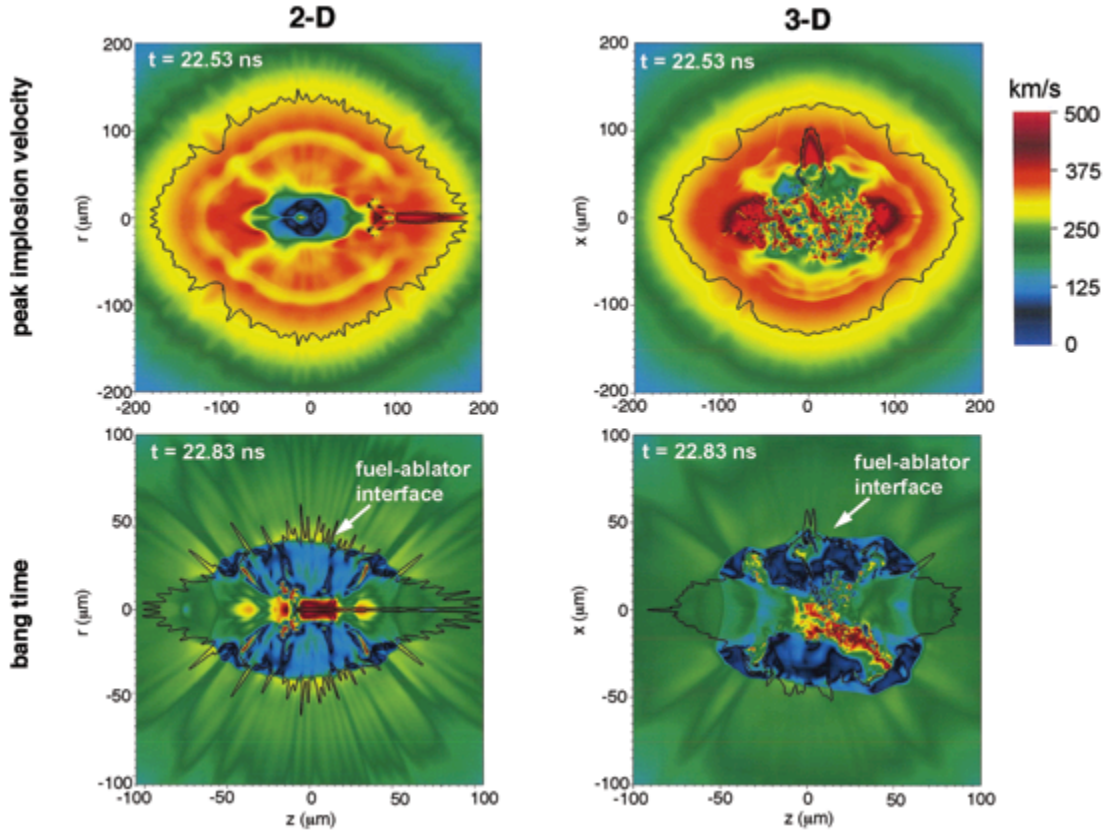
2-D
3-D
peak implosion velocity
bang time
t = 22.53 ns
t = 22.83 ns
fuel-ablator interface
km/s
500
375
250
125
0
r (μm)
x (μm)
z (μm)

Fig. 10.

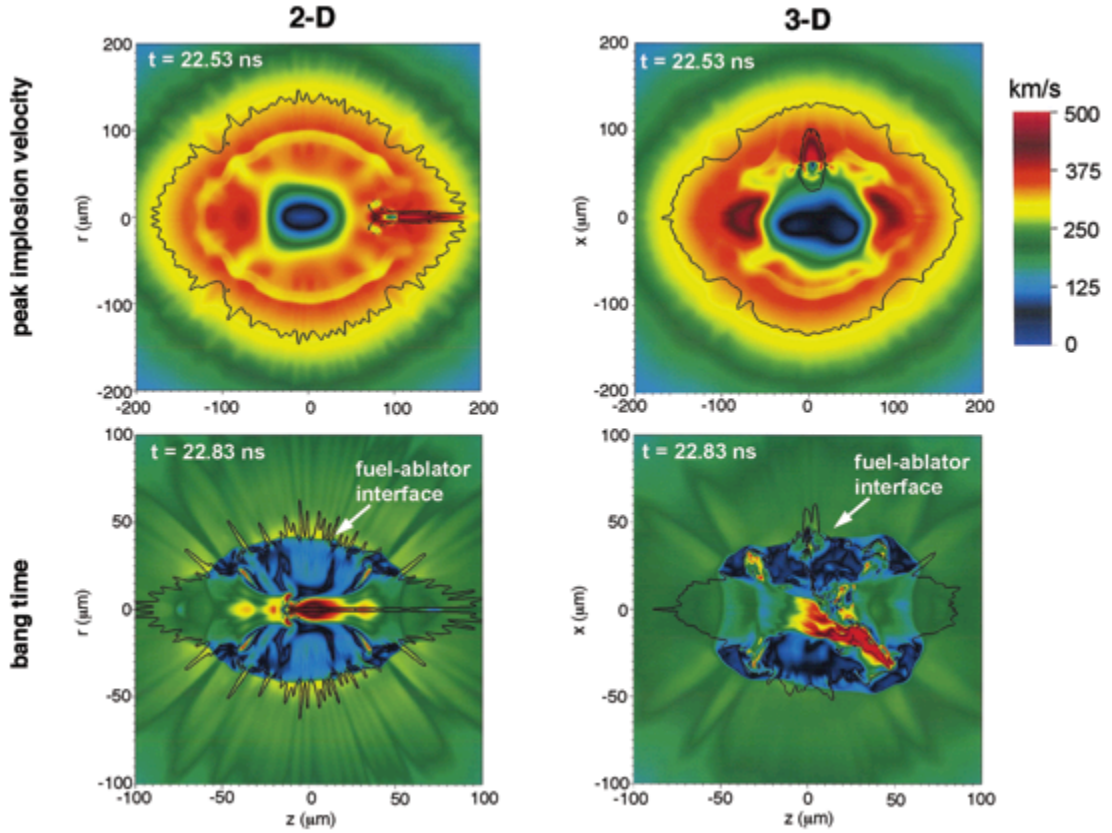
2-D
3-D
peak implosion velocity
bang time
t = 22.53 ns
t = 22.83 ns
fuel-ablator interface
km/s
500
375
250
125
0
r (μm)
x (μm)
z (μm)